We are IntechOpen,
the world's leading publisher of
Open Access books
Built by scientists, for scientists

4,800
Open access books available

122,000
International authors and editors

135M
Downloads

Our authors are among the

154
Countries delivered to

TOP 1%
most cited scientists

12.2%
Contributors from top 500 universities

BOOK
CITATION
INDEX
CLARIVATE ANALYTICS
INDEXED

WEB OF SCIENCE™

Selection of our books indexed in the Book Citation Index
in Web of Science™ Core Collection (BKCI)

Interested in publishing with us?
Contact book.department@intechopen.com

Numbers displayed above are based on latest data collected.
For more information visit www.intechopen.com

Multifunctional Characteristics of *B*-site Substituted BiFeO₃ Films

Hiroshi Naganuma

Department of Applied Physics, Graduate school of Engineering, Tohoku University
Japan

1. Introduction

In recent times, BiFeO₃ has been considered as an important material for the development of multifunctional devices because of its distinctive ferroelectric, magnetic, piezoelectric, and optical properties. These include a high Currie temperature of ferroelectricity (T_C~1100 K), (Venevtsev *et al.*, 1960), high Néel temperature of antiferromagnetism (T_N~650 K), (Kiselev *et al.*, 1963) lead-free piezoelectricity, and large flexibility in the wavelength of visible light region. These features make BiFeO₃ particularly applicable in the fields of ferroelectrics, magnetics, piezoelectrics, and optics; in addition, the cross correlation of these properties can be expected above room temperature (RT). [Fig. 1] BiFeO₃ has a perovskite-type crystal structure that is rhombohedrally distorted in the [111] direction and crystallized in the space group *R3c* [Fig. 2]. (Kubel *et al.*, 1990) The ferroelectric performance of BiFeO₃ is comparable to that of conventional ferroelectric materials such as Pr(Zr,Ti)O₃ (PZT) because BiFeO₃ exhibits excellent spontaneous polarization at RT. Theoretically, spontaneous polarization corresponds to crystal symmetry, wherein the rhombohedral and tetragonal BiFeO₃ structures are expected to show spontaneous polarizations of ≈100 μC/cm² in the [111] direction and ≈150 μC/cm² in the [001] direction, respectively. [Fig. 3(a)] (Ederer *et al.*, 2005) In fact, these theoretically predicted large spontaneous polarizations in BiFeO₃ are almost consistent with the experimental results [Figs. 3(b) and 3(c)] (Li *et al.*, 2004, Yun *et al.*, 2004), stating that BiFeO₃ is favorable for use in ferroelectric random access memory (FeRAM) applications. However, the practical application of BiFeO₃ thin films has been limited by their large leakage current density and large coercive field at RT, (Naganuma *et al.*, 2007, Pabst *et al.*, 2007) as a result, BiFeO₃ thin films easily undergo electrical breakdown when a large leakage current passes through them before the polarization is switched. Therefore, in order for BiFeO₃ films to find practical future application, the leakage current and/or coercive field of these films must be reduced. In term of magnetic properties, BiFeO₃ is antiferromagnetic with a *G*-type spin configuration; (Kubel *et al.*, 1990, Ederer *et al.*, 2005) that is, nearest neighbor Fe moments are aligned antiparallel to each other, and there is a sixfold degeneracy, resulting in an effective "easy magnetization plane" for the orientation of the magnetic moments within the (111) plane. It should be noted that the antiferromagnetic (111) plane is orthogonal to the ferroelectric polarization direction [111] in the rhombohedral structure. [Fig. 4(a)] The orientation of the antiferromagnetic sublattice magnetization is coupled through ferroelastic strain due to crystal symmetry, and it should always be perpendicular to the ferroelectric polarization [111] direction. Therefore, a polarization switch to either 71° or 109° should

change the orientation of the antiferromagnetic plane. This change in orientation would, however, not occur in the case of 180° to 180° ferroelectric polarization switching. [Fig. 4(b)-4(d)] In fact, experimentally, (Zhao *et al.*, 2006) the ferroelectric domain and antiferromagnetic domain in $BiFeO_3$ (100) epitaxial films are strongly coupled (magneto-electric (ME) coupling) in the orthogonal configuration, and the orientation of the antiferromagnetic plane is switched by a 109° switch in the ferroelectric domain. In effect, the magnetization configuration can be controlled by the application of an electric field through ferroelectric domain switching; by means of this mechanism, it is possible to realize voltage control of magnetic random access memory (V-MRAM). The use of V-MRAM can drastically reduce electrical consumption when compared with spin-MRAM which is operated by spin-polarized current. In terms of "how to detect the change of magnetization induced by ferroelectric domain switching", it can be seen that owing to Dzyaloshinskii-Moriya (DM) interaction, (Dzyaloshinskii, 1957, Moriya, 1960) the symmetry permits a canting of the antiferromagnetic sublattices, resulting in a local weak spontaneous magnetization. This magnetization is macroscopically canceled by a spiral spin structure caused by the rotation of the antiferromagnetic axis through the crystal with an incommensurately long-wavelength period of 62 nm. (Sosnowska *et al.*, 1982) This spiral spin structure might be suppressed in the film form of $BiFeO_3$ and the resulting magnetic moment is caused by a weak ferromagnetism of ~0.1 μ_B/Fe atom. However, this small magnetic moment is not suitable for application in devices such as spintronics because of the difficulty associated with the direction of a weak magnetic moment using a magnetic sensor, as well as the spin-filter effect. Therefore, in order to detect the change of magnetic states driven by ferroelectric domain switching (i) introduction of ferrimagnetic spin order into $BiFeO_3$ having a rombohedral structure or (ii) detection of the ferromagnetization change through exchange coupling with $BiFeO_3$ (Chu *et al.*, 2008) are the predominant candidates. In addition, the $BiFeO_3$ films show distinctive optical properties, as previously mentioned. $BiFeO_3$ has the highest flexibility among the oxide materials: a flexibility of 3.22 at a wavelength of 600 nm; this flexibility is expected to cross-correlate with the other physical properties. (Shima *et al.*, 2009) The details of the optical properties of $BiFeO_3$ films have been relegated to a subsequent
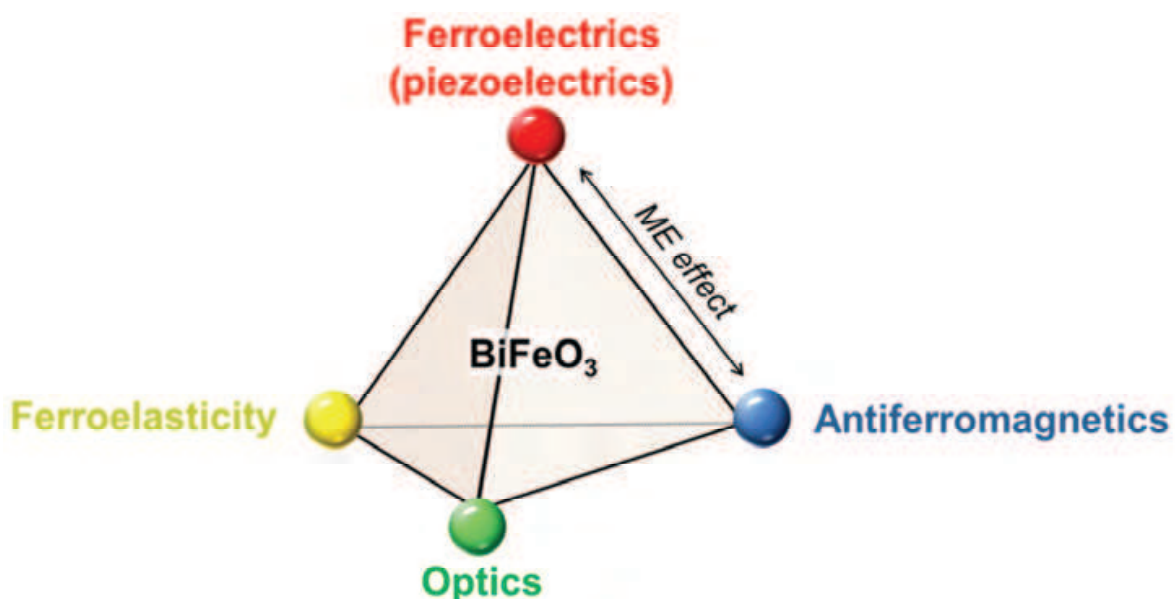

Fig. 1. Schematic illustration of cross correlation between ferroelectrcity (piezoelectrics), ferroelasticity, optical properties and antiferromagnetism for $BiFeO_3$.
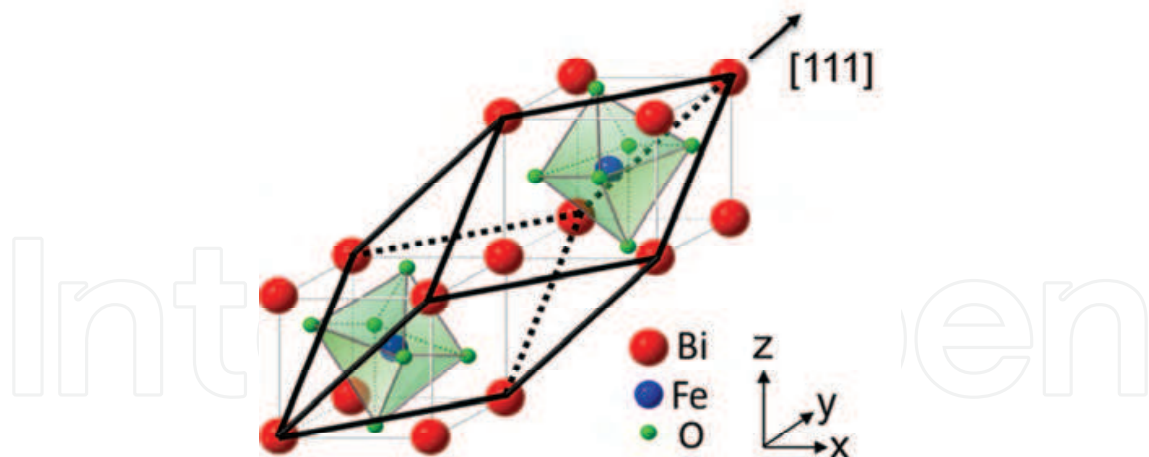
Fig. 2. Schematic drawing of the crystal structure of perovskite BiFeO₃ (space group: *R*3c). Two crystals along [111] direction are shown in the figure.
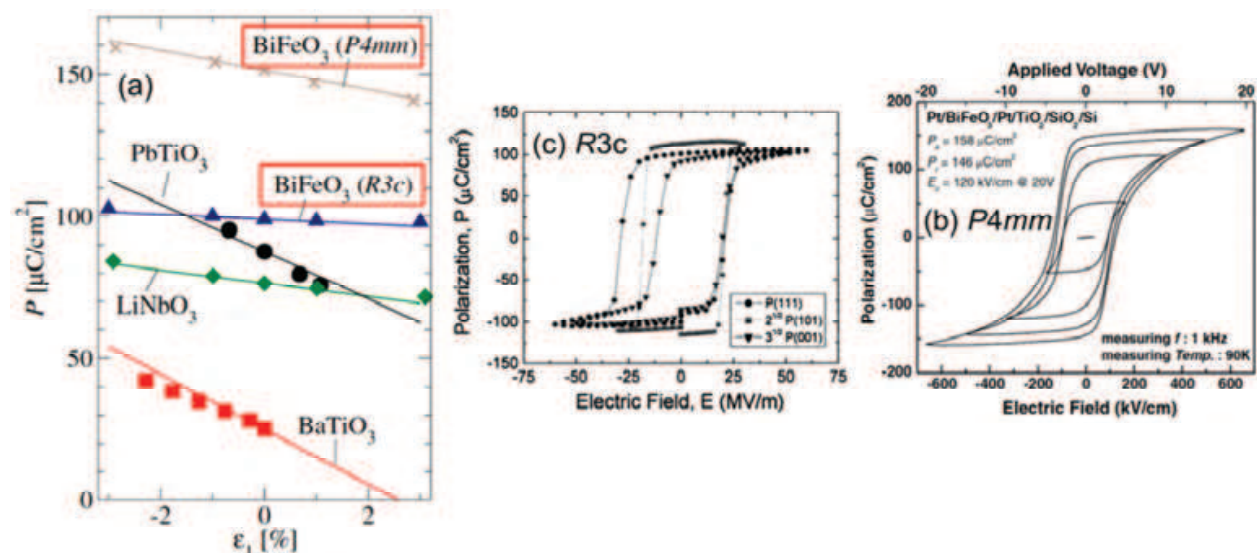

Fig. 3. (a) First-principle calculation of spontaneous polarization for BiFeO₃ with tetragonal (*P4mm*) and rhombohedral (*R3c*) symmetry. ε_1 indicates the epitaxial strain. Symbols represent directly calculated values. (Ederer *et al.*, 2005) (b) Experimental result of BiFeO₃ with tetragonal structure, and (c) with rhombohedral structure.

discussion. Based on these background considerations, the main focus of this chapter is the structure, ferroelectricity, and magnetism of BiFeO₃ films. In addition, we discuss the effect of the substitution of various 3*d* transition metals into the *B*-site of BiFeO₃ films on the films' structural, ferroelectric, and magnetic properties. We also propose a new multiferroic material having a ferrimagnetic spin order and large spontaneous polarization at RT. This chapter includes three sections. Section 1 presents the fundamental characteristics of pure BiFeO₃ films. Section 2 describes substitution of various 3*d* transition metals for Fe in BiFeO₃ films, in small amount (~5 at.%), in order to achieve ferrimagnetic spin ordering together with low leakage current density. Finally, in Section 3, we demonstrate the substitution of a large amount of Co (~58 at.%).
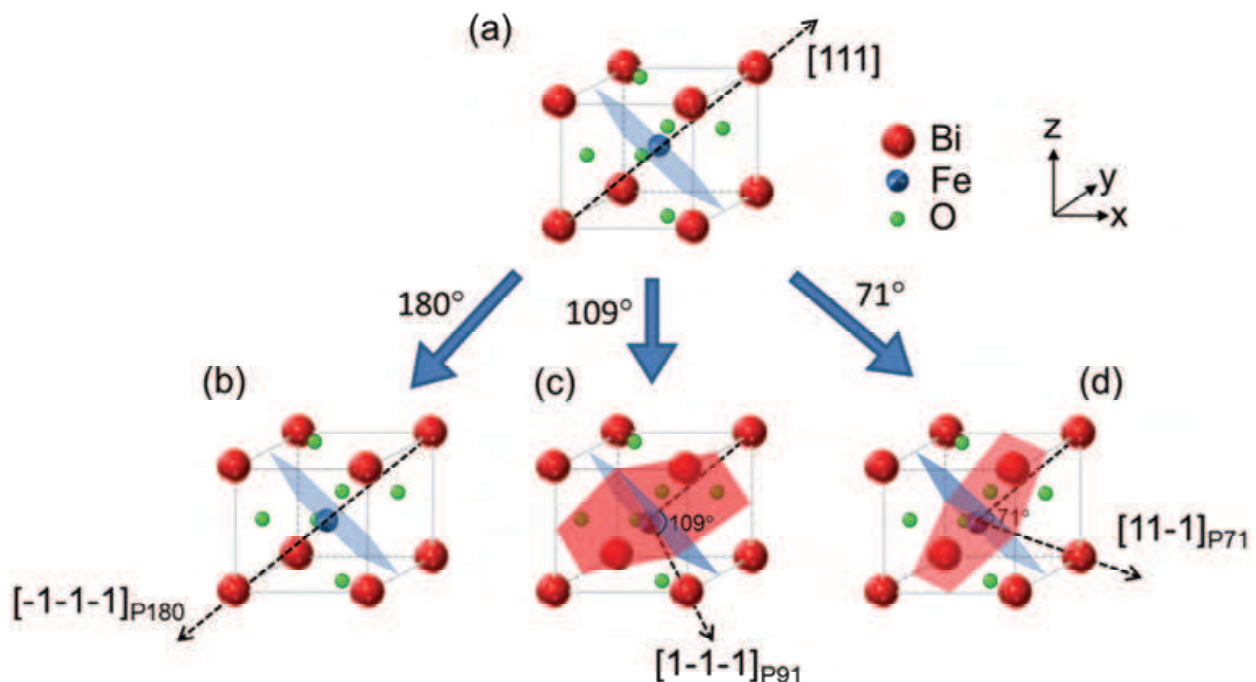
Fig. 4. Schematic illustration of cross correlation between ferroelectric polarization and antiferromagnetic plane. Antiferromagnetic plane was defined as the direction of magnetic moment of weak ferromagnetism due to DM interaction.

2. Structural, electronic, and magnetic properties of BiFeO₃ films

In order to elucidate the fundamental properties of $BiFeO_3$ films, here, we begin by systematically investigating the effect of annealing temperature on the structural, electrical, and magnetic properties of $BiFeO_3$ polycrystalline film. The results described in this section is based on our recent work as follows; Naganuma *et al.* TMRSJ, 2007, Naganuma *et al.* MT, 2007, Naganuma *et al.* IF, 2007, Naganuma *et al.* TUFFC, 2008, Naganuma *et al.* JJAP, 2008, Naganuma *et al.* APEX, 2008, Naganuma *et al.* JCSJ, 2010, Naganuma *et al.* JAP, 2011.

Polycrystalline $BiFeO_3$ films were prepared by a chemical solution deposition (CSD) method. The preparation processes are shown in Fig. 5 and can be summarized as follows: an enhanced-metal-organic-decomposition (E-MOD) solution (with stoichiometric composition Bi:Fe=1:1, 0.2 mol/l) was used as the precursor solution. The precursor solution was spin-coated onto Pt (150 nm)/Ti (5 nm)/SiO₂/Si (100) substrates at a rotation speed between 4000 and 6000 rpm for 50 s. Pt and Ti were deposited by r.f. magnetron sputtering using Ar gas at RT. The spin-coated films were dried at 150°C for 1 min and calcined at 350°C for 5 min. The spin coating and calcination processes were repeated 4-5 times, after which the films were sintered in air at 400 - 800°C for 10 min by rapid thermal annealing (RTA; ULVAC mila-5000). The films had a thickness of approximately 200 nm. The surface morphology of the films was observed by atomic force microscopy (AFM; SII SPI3800N) and scanning electron microscopy (SEM; JEOL JSM-6380). The crystal structure and orientation were confirmed by X-ray diffraction (XRD; PANalytical X'Pert MRD) with Cu-Kα radiation and transmission electron microscopy (TEM; JEOL JEM-2100F, JEOL JEM-3000F, LEO-922) working at 200 and 300 kV. The leakage current density was measured using a pico-ampere

meter (HP 4140B). The ferroelectric hysteresis (*P-E*) loop of the films was measured using a ferroelectric tester (aixACCT TF-2000, TOYO FCE-1A) with a single triangular pulse. Positive-Up-Negative-Down (PUND) measurement was also used for evaluating electrical properties. The magnetic properties were measured with a vibrating sample magnetometer (VSM; Tamakawa) at RT, and a superconducting quantum interference device (SQUID; Quantum design MPMS) magnetometer was used for the in-plane direction.
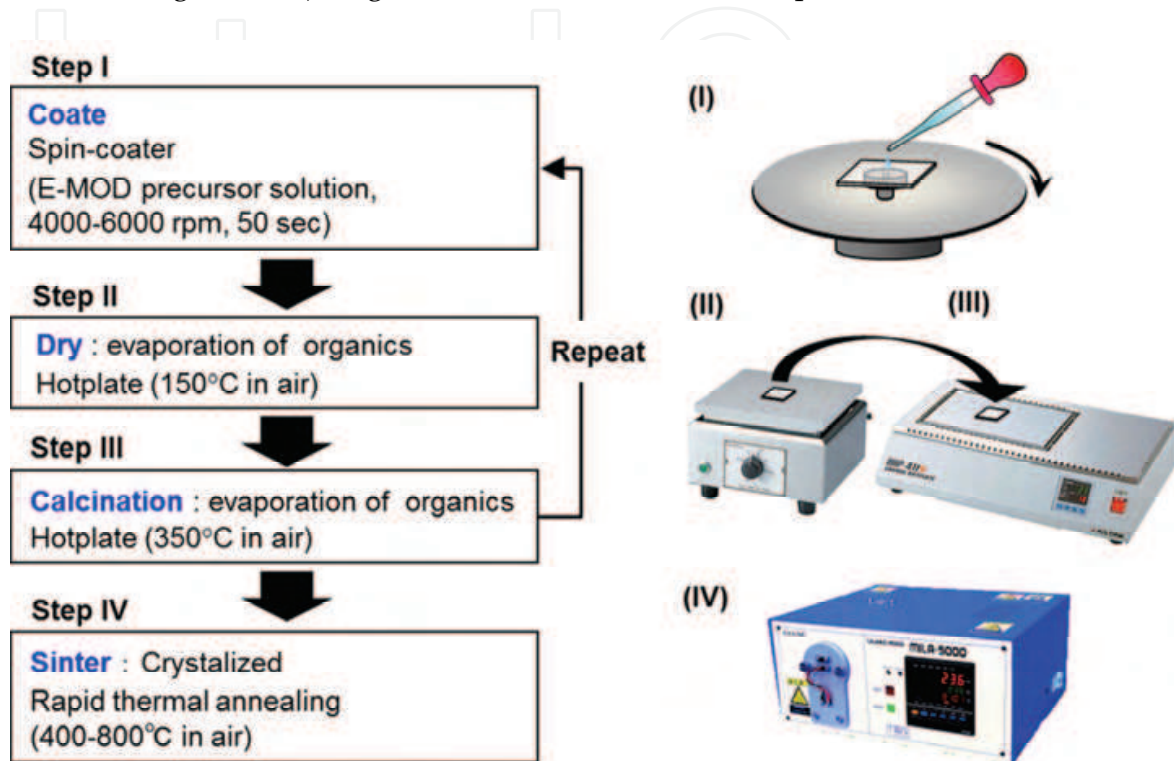

Fig. 5. Schematic illustration of preparation process using CSD.

Figure 6 shows the XRD profiles of BiFeO₃ films deposited on Pt/Ti/SiO$_2$/Si(100) substrates annealed at various temperatures. For each annealing temperature, a strong diffraction peak at 2θ = 39.8° was observed due to the Pt (111) plane. At an annealing temperature of 400°C, a weak diffraction peak was observed in the region of 2θ = 46°; however, it was not clear whether this diffraction peak originated from BiFeO₃ (024) at 2θ = 45.74° or Pt (200) at 2θ = 46.24°. Therefore, in order to clarify the origin of the diffraction peak in the region of 2θ = 46°, XRD analyses were undertaken for the Pt/Ti/SiO$_2$/Si(100) substrate only. On the basis of this experiment, the diffraction peak in the region of 2θ = 46° was identified as Pt (200) for the sample annealed at 400°C. Therefore, the structure of the film annealed at 400°C was amorphous or nanocrystalline. The formation of the polycrystalline BiFeO₃ films for annealing temperature above 450°C was indicated by the appearance of numerous diffraction peaks attributed to the BiFeO₃ structure above the stated temperature. The strong [111] orientation of the bottom Pt layer did not affect BiFeO₃ crystal growth. At annealing temperature above 700°C, secondary phases such as α-Fe$_2$O$_3$ and BiPt were formed. The observation of these phases indicates that the excess Fe formed α-Fe$_2$O$_3$ due to diffusion of Bi into the Pt electrode at high annealing temperatures. The indication is that the single phase of randomly oriented polycrystalline BiFeO₃ film was formed at annealing temperatures between 450 and 650°C.
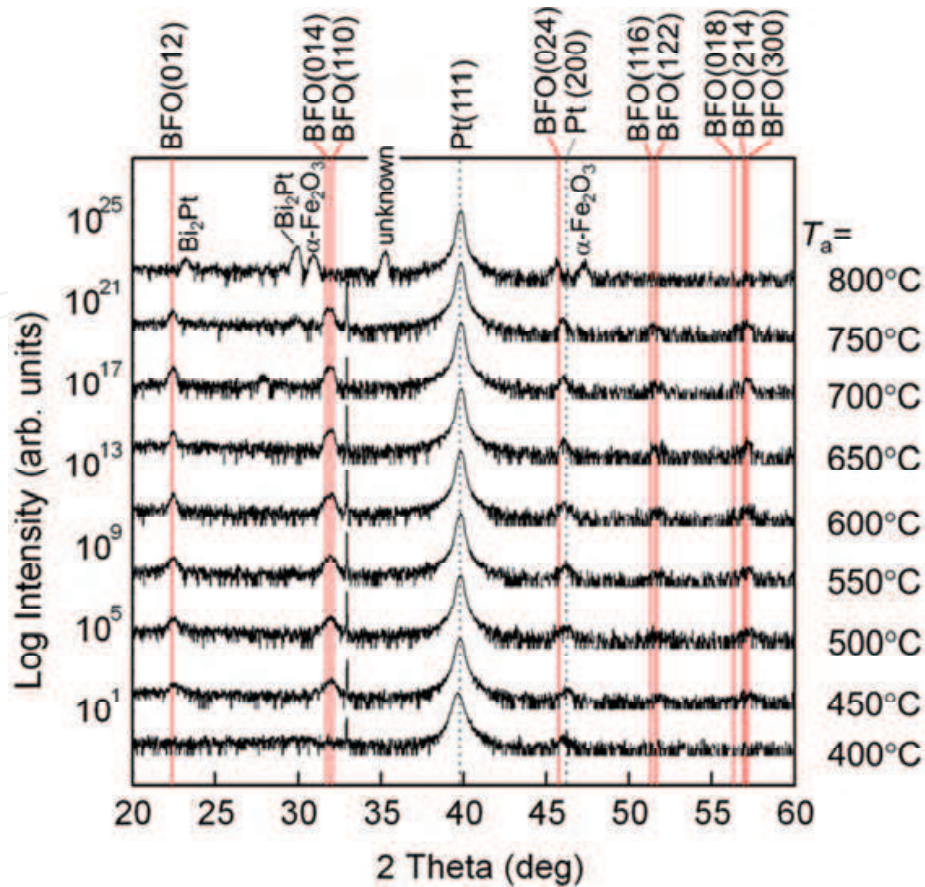
Fig. 6. XRD profiles of BiFeO$_3$ films deposited on Pt/Ti/SiO$_2$/Si(100) substrates annealed at various temperatures
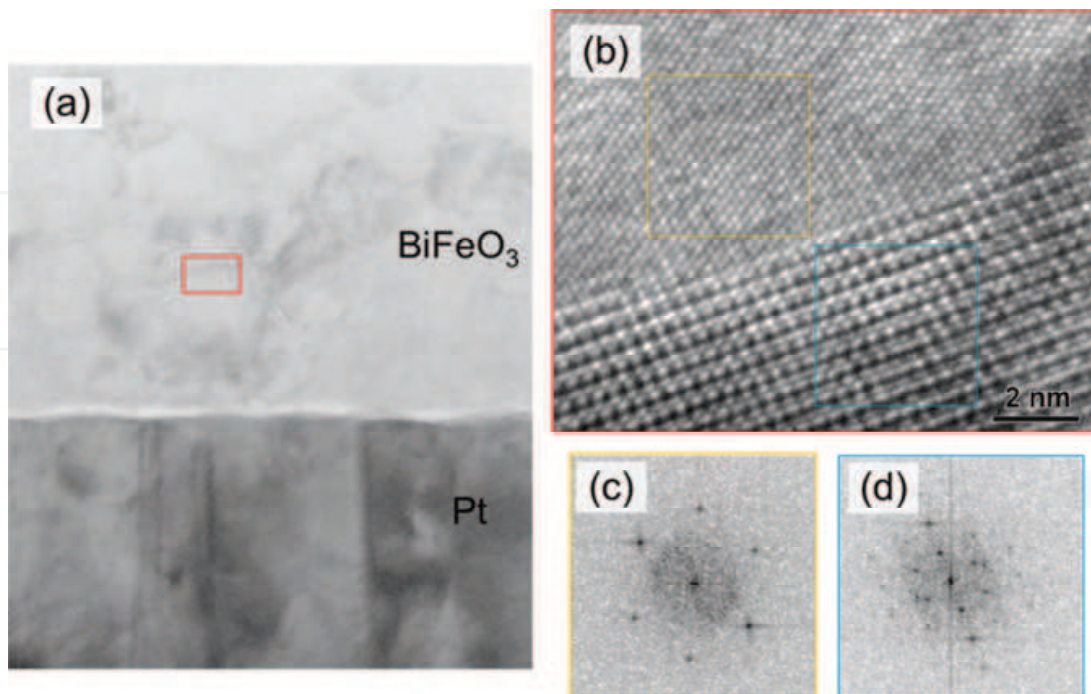

Fig. 7. Cross-sectional TEM images of polycrystalline BiFeO$_3$ films annealed at 550°C.
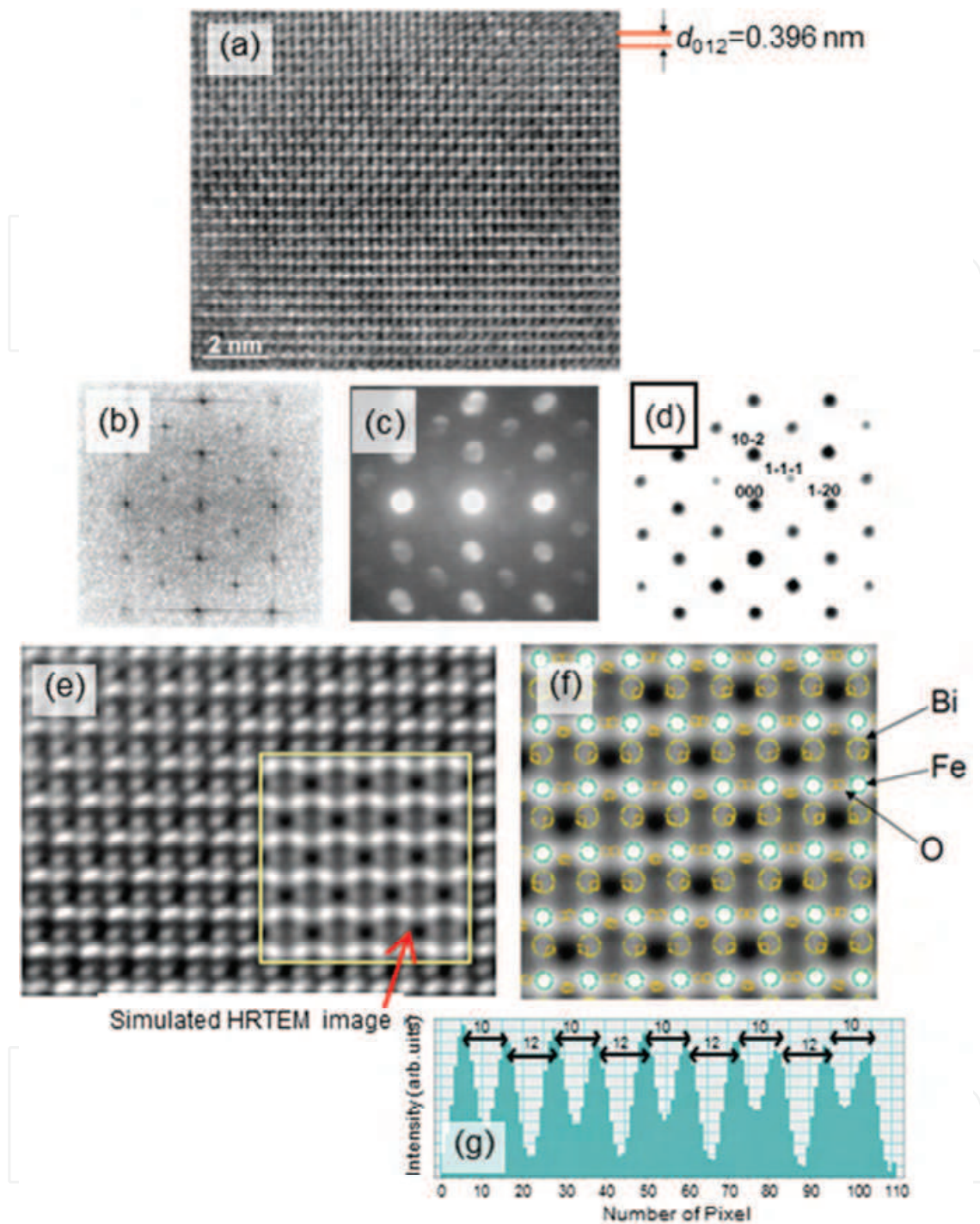
Fig. 8. (a) HRTEM image, (b) corresponding FFT pattern image, (c) NBD pattern, (d) simulated electron diffraction pattern, (e) simulated lattice fringe image embedded in observed HRTEM image, (f) atom position , and (g) distance between atoms.

Cross-sectional TEM observation was used to investigate the quality of the polycrystalline BiFeO₃ films annealed at 550°C. The observation, presented in Fig 7(a) indicates that the bottom Pt layer shows the (111) texture structure, which is consistent with the XRD profiles. High-resolution (HR) TEM was used to investigate the grain boundary phases in the polycrystalline structure within the square area outlined in Fig. 7(a). The HRTEM image of

the grain boundary [Fig. 7(b)] and fast Fourier transform (FFT) pattern from two grains [Fig. 7(c), 7(d)] are shown. These investigations show that high quality polycrystalline $BiFeO_3$ films were successfully fabricated by means of the CSD method

In the case of $BiFeO_3$, crystal symmetry exerts a strong influence on the ferroelectric polarization; (Ederer *et al.*, 2005) therefore, the crystal symmetry of $BiFeO_3$ was determined by simulation of the HRTEM images and nanobeam diffraction (NBD) patterns. Figure 8(a) shows the HRTEM image (a), corresponding FFT pattern (b), NBD pattern (c), simulated electron diffraction pattern (d), simulated lattice fringe image embedded in the observed HRTEM image (e), atom position (f), and distance between atoms (g). The HRTEM image contains periodic lattice fringes along the [012] direction with spacings of approximately 0.396 nm which is in good agreement with Kubel's report. (Kubel *et al.*, 1990) The electron diffraction pattern was simulated using the MacTEMPAS computer program by applying the multislice method (Kirkland *et al.*, 1998) and using the lattice parameters of the rhombohedral *R*3c and the tetragonal *Pbmm* lattices. (Kubel *et al.*, 1990, Wang *et al.*, 2003, Yun *et al.*, 2004) A comparison of the simulated electron diffraction pattern with the NBD and FFT patterns shows that the $BiFeO_3$ layer has a rhombohedral *R*3c structure. The simulated lattice fringe image of *R*3c corresponded exactly to the HRTEM image. The position of the atoms in the HRTEM image and the periodicity of the atoms based on *R*3c symmetry are indicated in Fig. 8(d) and 8(e).

Figure 9 shows the AFM and SEM images of the $BiFeO_3$ films as a function of annealing temperature. At temperatures of 400 and 450°C [Fig. 9(a) and 9(b)], a homogeneous surface was formed and no obvious grains were detected for the sample annealed at 400°C. The appearance of grains was observed in samples annealed at temperatures above 450°C. In the wide area AFM images, very little variation in the grain size was seen with an increase in the annealing temperature between 450 and 750°C. In contrast, the expanded AFM images show grains with sizes of several tens of nanometers, indicating that the micron sized grains consisted of an agglomeration of small grains, several tens of nanometers in diameter. [Fig. 9(c)] The size of the smaller grains increased as the annealing temperature increased. In particularly, there was a drastic increase in the size of the smaller grains above 700°C. The sample annealed at 800°C could not be analyzed using AFM because the specimen was easily stripped away from the substrate. Therefore, the surface morphology of this specimen was observed using SEM. [Fig. 9(i)] Square-shaped grains were observed after annealing at 800°C; this can be identified as the secondary phases of α-Fe_2O_3 and BiPt. These observations indicate that the microstructure of $BiFeO_3$ films is drastically influenced by the annealing temperature.

There are many reports that focus on leakage current density; however, only a few of these have discussed the mechanism underlying the leakage current. Hence, the topic of leakage current density is still open to discussion and can be considered an important issue from the viewpoint of memory applications. Herein, the leakage current mechanism operating in the $BiFeO_3$ film is discussed as a function of the annealing temperature. Figure 10 shows (a) the leakage current density (*J*) v.s. electric field (*E*), (b) Schottky emission plot (log *J* v.s. $E^{1/2}$), (c) Ohmic plot (double logarithm plots), (d) Fowler-Nordheim plot ($\log(J/E^2)$ vs $1/E$), (e) Poole-Frenkel plot ($\log(J/E)$ v.s. $E^{1/2}$) plots, and (f) space-charge-limited current ($\log(J/E)$ v.s. log *V*) for the $BiFeO_3$ film annealed at various temperatures. (Naganuma & Okamura, JAP 2007, Naganuma *et al.*, IF 2007) The measurement was carried out at RT. As shown in Fig. 10(a), the leakage current density of $BiFeO_3$ films tended to increase with increasing annealing

temperature. Careful observation of the slopes of the curves shows three steps corresponding to three kinds of leakage current mechanisms. First, we discuss the interfacial limited leakage current mechanism, taking into consideration Schottky emission. Using Schottky emission, the relative permittivity and barrier height were estimated to be 0.4 and 0.6 eV, respectively [Fig. 10(b)]. On the other hand, the inclination at a low electric field in the double logarithm plots, as shown in Fig. 10(c) was around 1.1–1.2. Compared to the Schottoky-emission conduction, Ohmic conduction seems to be adaptable at low electric field. The inclination at a high electric field in the double logarithm plots in Fig. 10(b) was around 2, indicating that the leakage current behavior at high electric field was dominated
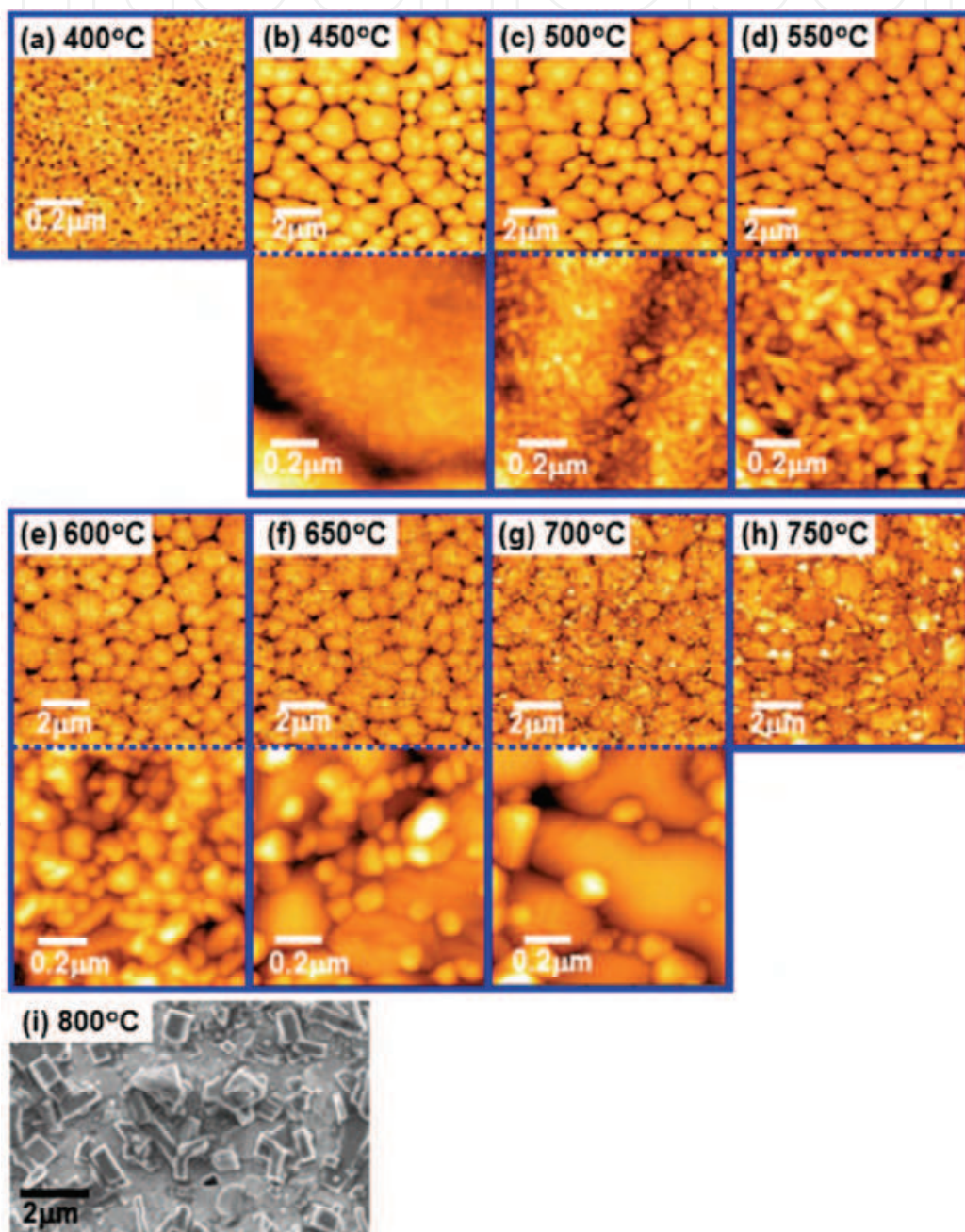

Fig. 9. AFM and SEM images of the BiFeO₃ films as a function of annealing temperature.
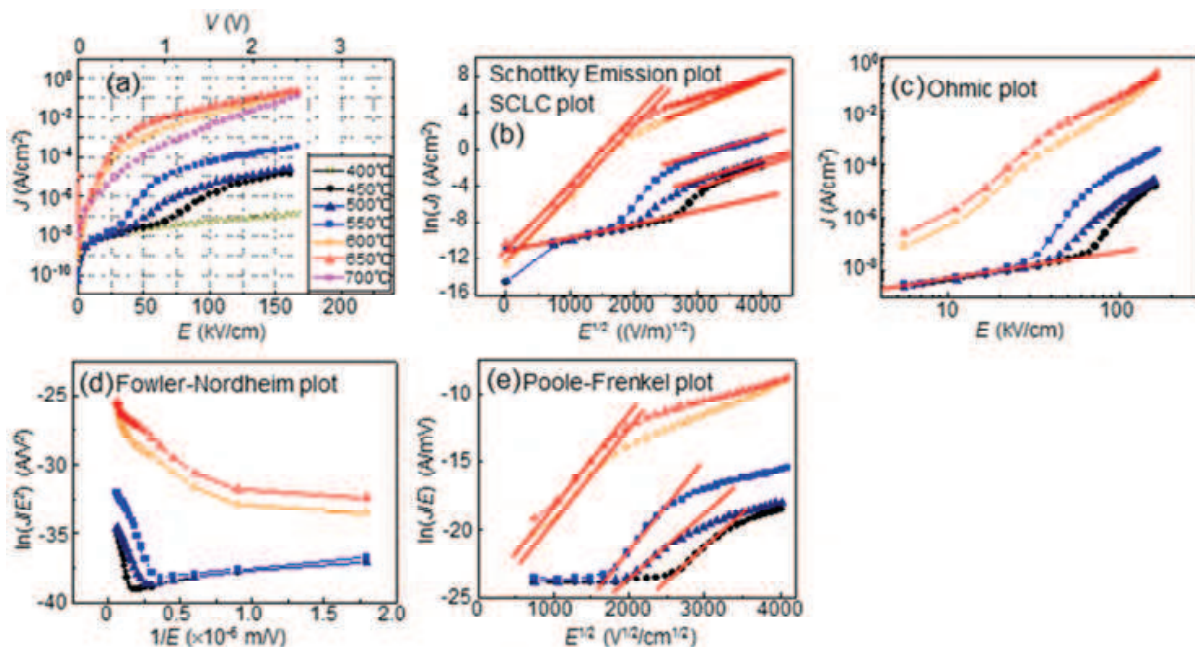
Fig. 10. Leakage current mechanism for BiFeO$_3$ at various annealing temperatures.

by space-charge-limited current (SCLC). Next, we discuss the leakage current mechanism before the start of the SCLC. The barrier height deduced from the Fowler-Nordheim equation was around 0.019 eV [Fig. 10(d)]. This barrier height is quite small for Fowler-Nordheim tunneling conduction. The relative permittivity calculated using the Poole-Frenkel equation was around 0.1–0.2 [Fig. 10(e)]. Here, it is though that the leakage current mechanism changed as follows: Ohmic conduction occurred at a low electric field; Poole-Frenkel trap limited conduction appeared as the electric field increased; and SCLC was activated at a high electric field.

Figure 11 shows the *P-E* hysteresis loops of the BiFeO$_3$ films annealed at various temperatures. The *P-E* hysteresis loop was measured at RT using a frequency of 2 kHz
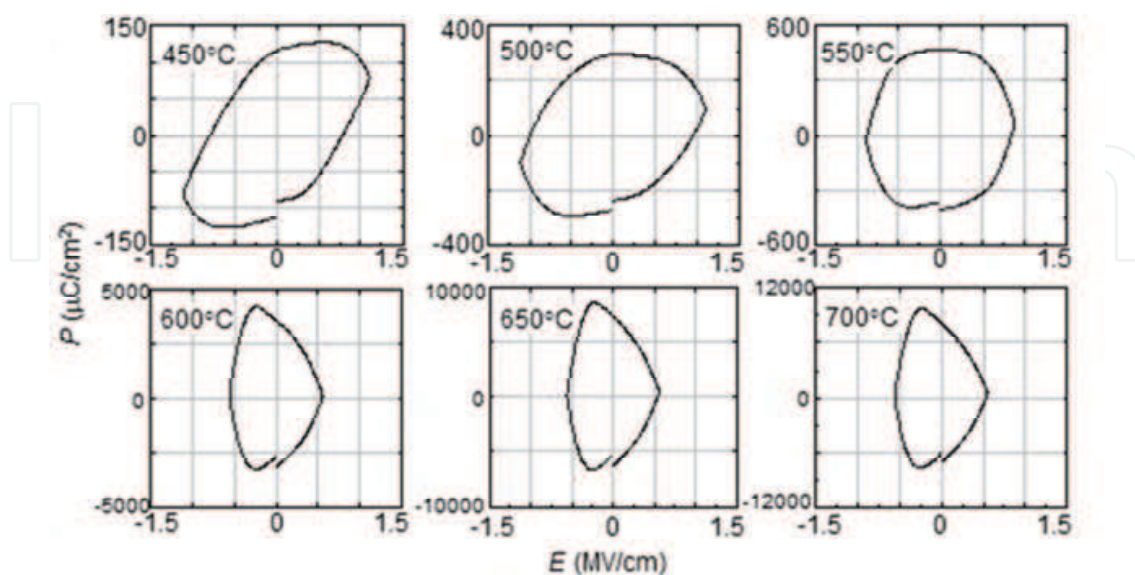

Fig. 11. Ferroelectric (*P-E*) hysteresis loops of the BiFeO$_3$ films annealed at various temperatures.
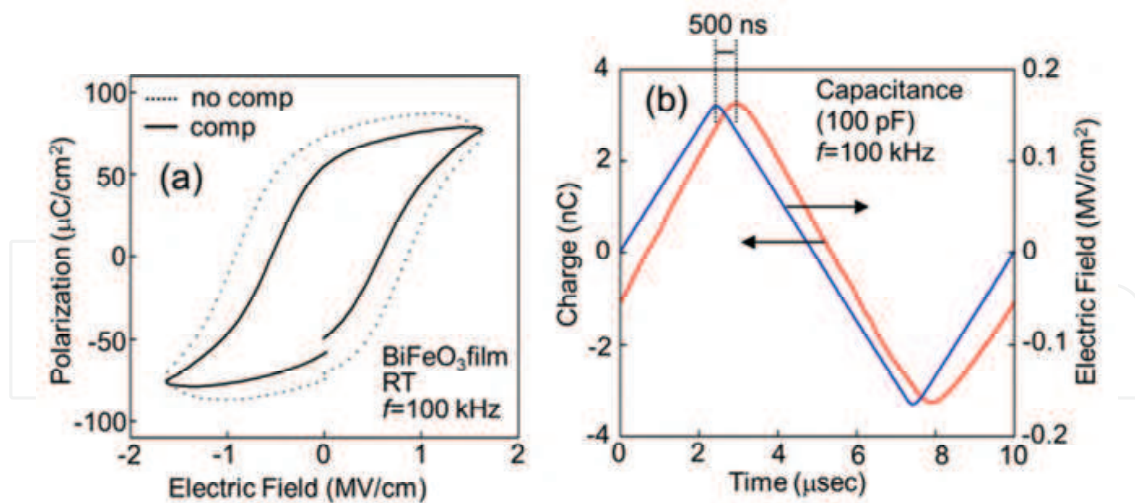
Fig. 12. (a) Compensation of phase delay using high frequency 100 kHz system. Solid line indicates the use of phase-delay compensation, and the dotted line indicates the case in which there was no compensation. (b) changes in the electric field and polarization against time for standard capacitor.

(aixACCT TF-2000). The *P-E* hysteresis loop has an unsaturated, loose shape even in the case of the BiFeO₃ film annealed at 450°C, which is indicative of a low leakage current density.

Two methods were employed in order to reduce the influence of leakage current density on the *P-E* hysteresis measurements: (i) a high frequency system was used and (ii) measurements were taken at low temperatures. Figure 12(a) shows the *P-E* hysteresis loops for BiFeO₃ film annealed at 450°C; the loops were obtained using the 100 kHz high frequency system. The solid line indicates the use of phase-delay compensation, and the dotted line indicates the case in which there was no compensation.

The compensation of phase delay from the high voltage amplifier and circuit cable was estimated by using a standard capacitor of 100 pF. The changes in the electric field and polarization against time are shown in Fig. 12(b). Changes in polarization appear to be delayed with respect to the changes in the applied electric field by approximately 500 nsec. When a phase delay compensation of 500 nsec was applied, the shape of the *P-E* hysteresis loop was improved to high squareness when compared with the low frequency measurement system, as shown in Fig. 11. The details of the compensation method are addressed elsewhere (Naganuma *et al.*, JCSJ 2010).

Figure 13 show the *P-E* hysteresis loops for BiFeO₃ films annealed at various temperatures, measured at RT using a high frequency 100 kHz system. For the BiFeO₃ films annealed at 400°C, the paraelectrics due to amorphous structure was observed. The *P-E* hysteresis begins to be observed from 450°C and a relatively high remanent polarization of 80-90 $\mu C/cm^2$ was obtained for the BiFeO₃ film annealed at 500°C. However, it seems that leakage current still influences the shape of the hysteresis loops for films annealed at high temperatures. Above 600°C, the *P-E* loops assume an unsaturated, loose shape and spontaneous polarization cannot be estimated. Figure 13(h) shows the electric field (*E*) dependence of remanent polarization (P_r) estimated from the *P-E* hysteresis loops. The P_r increased with increasing electric field and there was no clear tendency to saturate. It can thus be seen that the influence of leakage current on the *P-E* hysteresis loops was clearly reduced by increasing the measurement frequency.
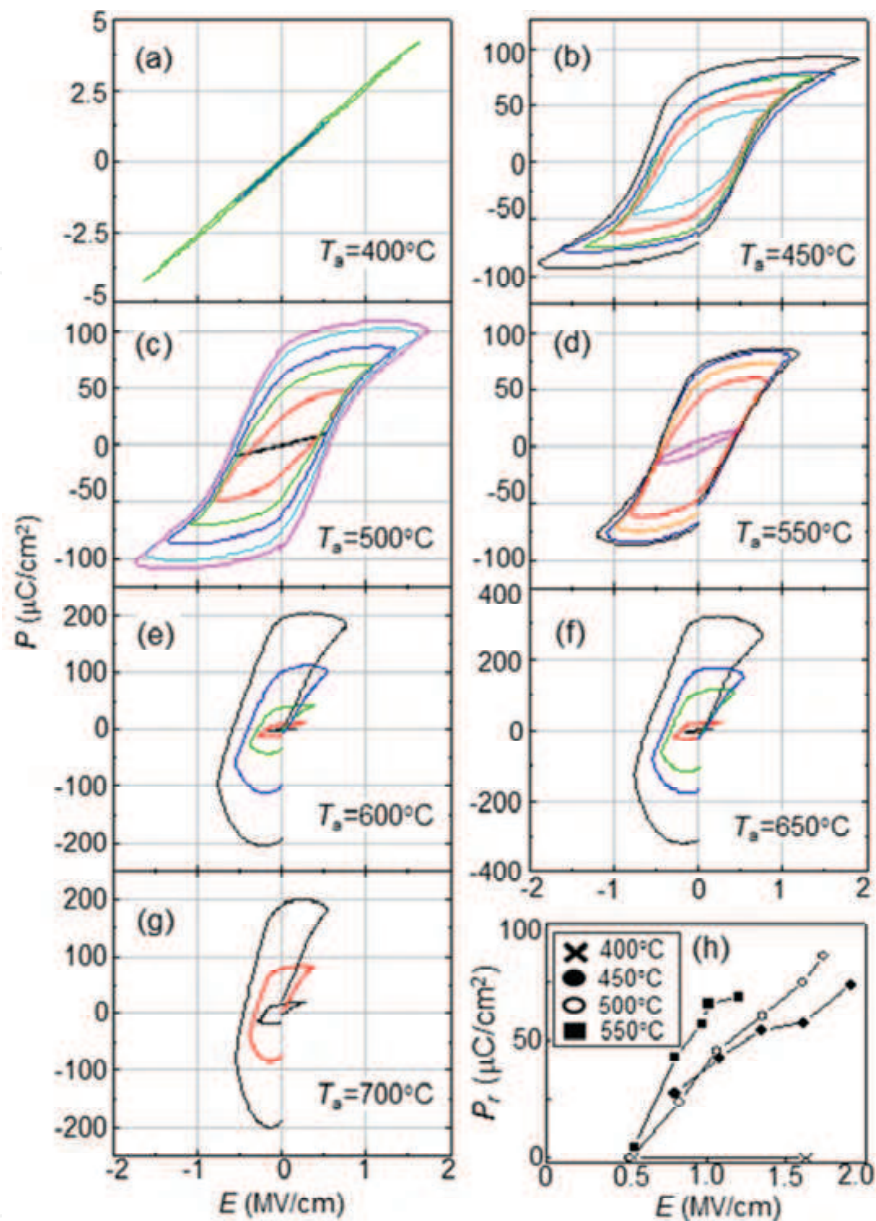
Fig. 13. *P-E* hysteresis loops measured at RT using high frequency 100 kHz system for BiFeO₃ films annealed at various temperatures.

Figure 14 shows the *P-E* hysteresis loops for BiFeO₃ films annealed at various temperatures, measured at -183°C using a measurement frequency of 1 kHz. At -183°C, the leakage current density was significantly decreased to below 1.0×10^{-8} A/cm² at 0.1 MV/cm; therefore, the influence of leakage current density on the ferroelectric measurement could be excluded. By decreasing the measurement temperature, the *P-E* hysteresis loops could be observed for the samples annealed in the temperature range between 450 and 750°C. No ferroelectricity was observed at the annealing temperature of 800°C due to the disappearance of the BiFeO₃ phase. The shape of the *P-E* hysteresis loops varied for each annealing temperature. Double *P-E* hysteresis loops were observed for the samples annealed at 450°C, whereas the shape of the *P-E* hysteresis loop for the sample annealed at 500°C was insufficiently saturated. This is

because the electric coercive field was high for the sample annealed at the lower temperature, and it was not enough to saturate the polarization by the electric field at around 1.3 MV/cm. The remanent polarization and electric coercive field as a function of the annealing temperature are summarized in Fig. 14(g). The remanent polarization of the BiFeO₃ films increased linearly with increasing annealing temperature up to 650°C and decreased above the annealing temperature of 700°C. The electric coercivity field of the BiFeO₃ films decreased as the annealing temperature increased. The highest remanent
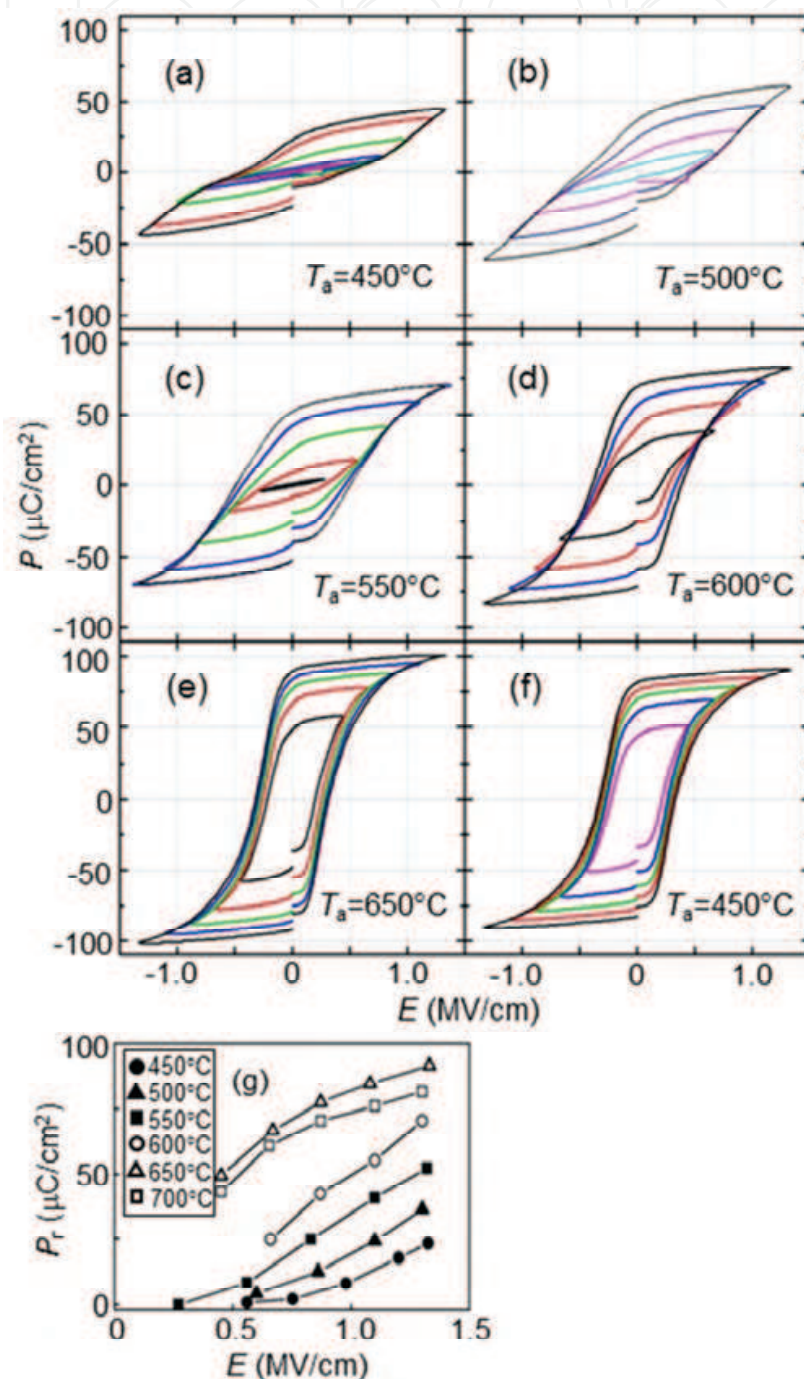

Fig. 14. *P-E* hysteresis loops of BiFeO₃ films annealed at various temperatures, measured at -183°C.

polarization, as well as the lowest electric coercive field of the $BiFeO_3$ film appeared at the annealing temperature of 650°C. The remanent polarization and the electric coercive field were 89 $\mu C/cm^2$ and 0.31 MV/cm, respectively, which are be comparable to the recent reports of high remanent polarization. These results reveal that the ferroelectric properties such as remanent polarization and the electric coercive field of the $BiFeO_3$ films are strongly affected by the annealing temperature of the CSD processes even though single phase, the polycrystalline $BiFeO_3$ films were formed.

Figure 15 shows the magnetization (*M-H*) curve at RT for the $BiFeO_3$ film annealed at 650°C. The magnetization increased linearly at high magnetic field due to the anitiferromagnetic spin structure. In the zero fields region, nonlinear hysteresis with a very small remanent magnetization was observed, which might be considered to be the weak ferromagnetism due to DM interaction (Dzyaloshinskii, 1957, Moriya, 1960) or strain induced magnetization. Interestingly, non-linearity is often reported near the zero fields for the film form of $BiFeO_3$; (Kiselev *et al.*, 1963, Naganuma *et al.*, TUFFC 2008, Yun *et al.*, 2004, Bai *et al.*, 2005) however, non-linearity has not been observed in the case of bulk $BiFeO_3$. (Bai *et al.*, 2005, Lebeugle *et al.*, 2007) This means that the non-linearity of the *M-H* curves is mainly affected by strain-induced changes of the spiral structure in the film. There are several reports which discuss the strain induced changes of the spiral structure in $BiFeO_3$ films. However, the details of the process are still debatable.
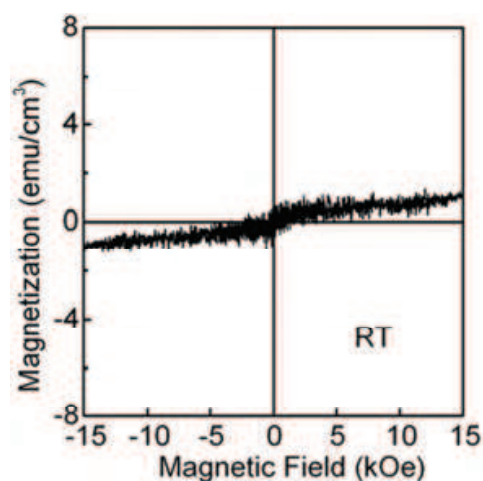

Fig. 15. Magnetization (*M-H*) curve at RT for $BiFeO_3$ film annealed at 650°C.

3. Effect of *B*-site substitution of Cr, Mn, Co, Ni, and Cu for Fe in $BiFeO_3$ on structural, electrical and magnetic properties

In the second section, single phase of polycrystalline $BiFeO_3$ films were successfully fabricated on $Pt/Ti/SiO_2/Si(100)$ substrates, and a high polarization of 89 $\mu C/cm^2$ with a switching field of 0.31 MV/cm was obtained at -183°C for films annealed at 650°C. However, the large leakage current, relatively large switching field of polarization, and antiferromagnetic spin configuration of $BiFeO_3$ films make it difficult to use these films in novel electrical applications such as spintronics devices. In this section, engineering of these physical properties is investigated by substitution of Fe in $BiFeO_3$ with various 3*d* transition metals. (Naganuma *et al.*, APL 2008, Naganuma *et al.*, JAP 2008, Naganuma *et al.*, JE 2009, Naganuma *et al.*, JMSJ 2009)

Cr, Mn, Co, Ni, and Cu substituted BiFeO$_3$ films (200 nm in thickness) were fabricated by the CSD method onto Pt/Ti/SiO$_2$/Si (100) substrates followed by post annealing in air at 650°C for 10 min. The composition of the E-MOD was adjusted as follows: Bi(Fe$_{0.95}$$M_{0.05}$)O$_3$ where M = Cr, Mn, Co, Ni, and Cu. The film structure was confirmed by the θ/2θ XRD pattern. The ferroelectric properties were measured using ferroelectric testers (TOYO Corporation: FCE-1A for RT and aixACCT: TF-2000 for -183°C). The leakage current was measured using a picoampere meter and the pulse response forms of the PUND measurement. The details of the estimation method are discussed elsewhere (Naganuma *et al.*, APEX 2008). The magnetic properties were measured using a VSM at RT for the in-plane direction.

Figure 16(a) shows the XRD profiles of Cr, Mn, Co, Ni, and Cu of 5 at. % substituted BiFeO$_3$ films: [Bi($M_{0.05}$Fe$_{0.95}$)O$_3$, M= Cr, Mn, Co, Ni, and Cu]. Diffraction peaks caused by the BiFeO$_3$ structure were observed, indicating the formation of a polycrystalline structure. The (012) diffraction peak of the Co-substituted BiFeO$_3$ film was stronger than those of the other substitutive metals; this implies the formation of a 012-textured structure. In the case of Cr-substituted BiFeO$_3$, a secondary phase of Bi$_7$CrO$_{12.5}$ was formed in addition to the BiFeO$_3$ phase.
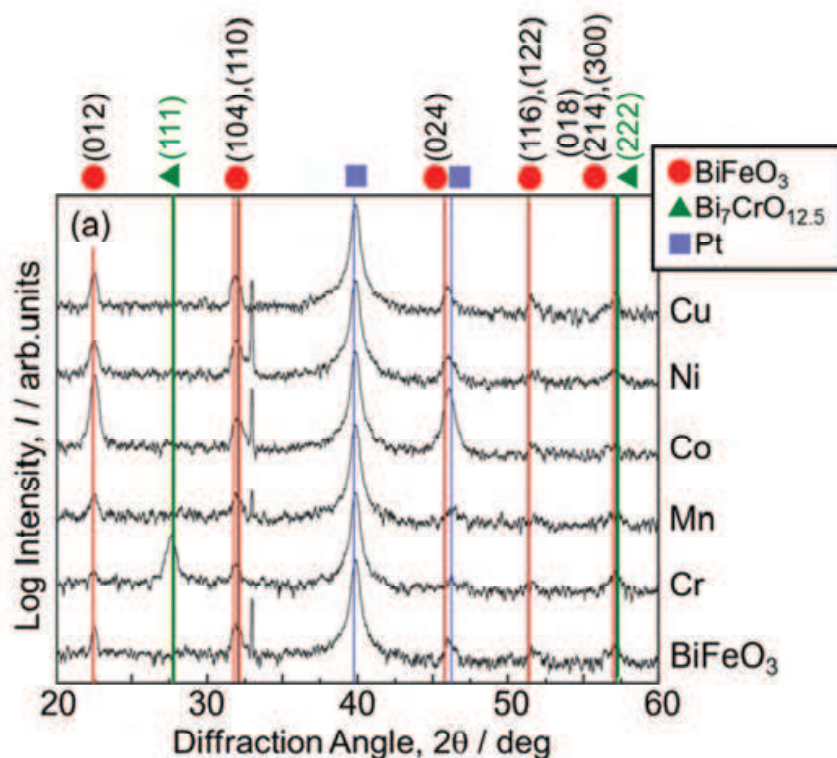

Fig. 16. XRD profiles of Cr, Mn, Co, Ni, and Cu of 5 at. % substituted BiFeO$_3$ films [Bi($M_{0.05}$Fe$_{0.95}$)O$_3$, M= Cr, Mn, Co, Ni, and Cu].

Figure 17 shows the leakage current density of Bi($M_{0.05}$Fe$_{0.95}$)O$_3$ films measured with the picoampere meter at RT. The leakage current density of the Ni-substituted BiFeO$_3$ film could not be precisely evaluated because of a considerably high leakage current. The leakage current density of the pure BiFeO$_3$ film increased more rapidly than those of the films with substitutions in response to increases in the electric field. However, even for the

transmission metal (TM) substituted films, it was difficult to measure the leakage current density above 0.2 MV/cm using the picoampere meter because of dielectric breakdown. In order to evaluate the leakage current density at higher electric fields, the leakage current density was estimated from the pulse response forms of the PUND measurements. In this way, the leakage current at high electric field can be measured by the reduction in the Joule heat damage. (Naganuma *et al.*, APEX 2008) An electric field more than 0.36 MV/cm could be applied, which is higher than that measured by the picoampere meter. Figure 17(b) shows the leakage current density estimated from the response forms of the up pulse. The leakage current density of the Ni-substituted BiFeO$_3$ film could also be measured by this method, and it was found to be considerably higher than that of the pure BiFeO$_3$ film. This indicates that the PUND method can be used for materials with a high leakage current density. The substitutions of Mn, Co, and Cu to the BiFeO$_3$ films effectively reduced the leakage current density in the high electric field region.
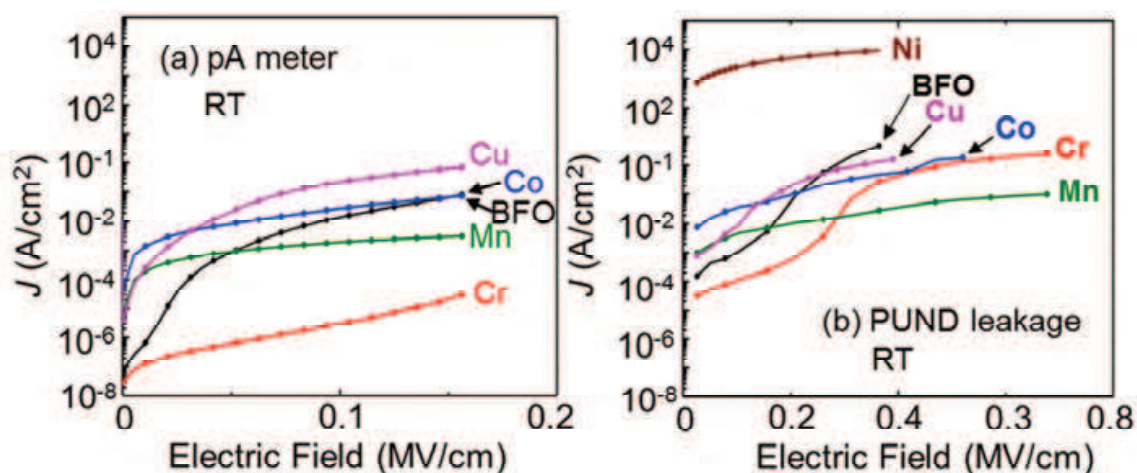
Fig. 17. (a) Leakage current density of Bi($M_{0.05}$Fe$_{0.95}$)O$_3$ films measured with the picoampere meter, and (b) by PUND measurement.

Figure 18 shows the ferroelectric hysteresis loops of the Bi($M_{0.05}$Fe$_{0.95}$)O$_3$ films measured with a 100 kHz driving system at RT using the ferroelectric tester, and those measured at -183°C using a 2 kHz driving system. Ferroelectric hysteresis loops could not be observed for the Ni-substituted BiFeO$_3$ film. The pure BiFeO$_3$ film showed an expanded hysteresis loop at RT [Fig. 18(a)], which could be attributed to the leakage current component. The squareness of the ferroelectric hysteresis loops was clearly improved by the substitution of Mn, Co, and Cu to the BiFeO$_3$ films. This squareness is attributed to the reduction in the leakage current density in the high electric field region. Although the leakage current density is reduced by the substitution of Mn, Co, and Cu, it is still difficult to apply a high electric field at RT. Therefore, the ferroelectric hysteresis loops were measured at -183°C using the 2 kHz driving system [Fig. 18(b)]. At -183°C, the leakage current density was considerably lower than the inversion current due to domain switching, as inferred from the current response of the PUND measurements. In fact, the ferroelectric hysteresis loops did not expand and showed high squareness at -183°C. E_c versus E plots [Fig. 18(c)] show that the E_c was reduced by the substitution of Co and Cu. In contrast, the substitution of Mn and Cr to the BiFeO$_3$ films produced a higher E_c compared to the pure BiFeO$_3$ film. In the Co- and Cu-substituted BiFeO$_3$ films, the P_r versus E plots [Fig. 18(d)] almost overlapped up to 1.3
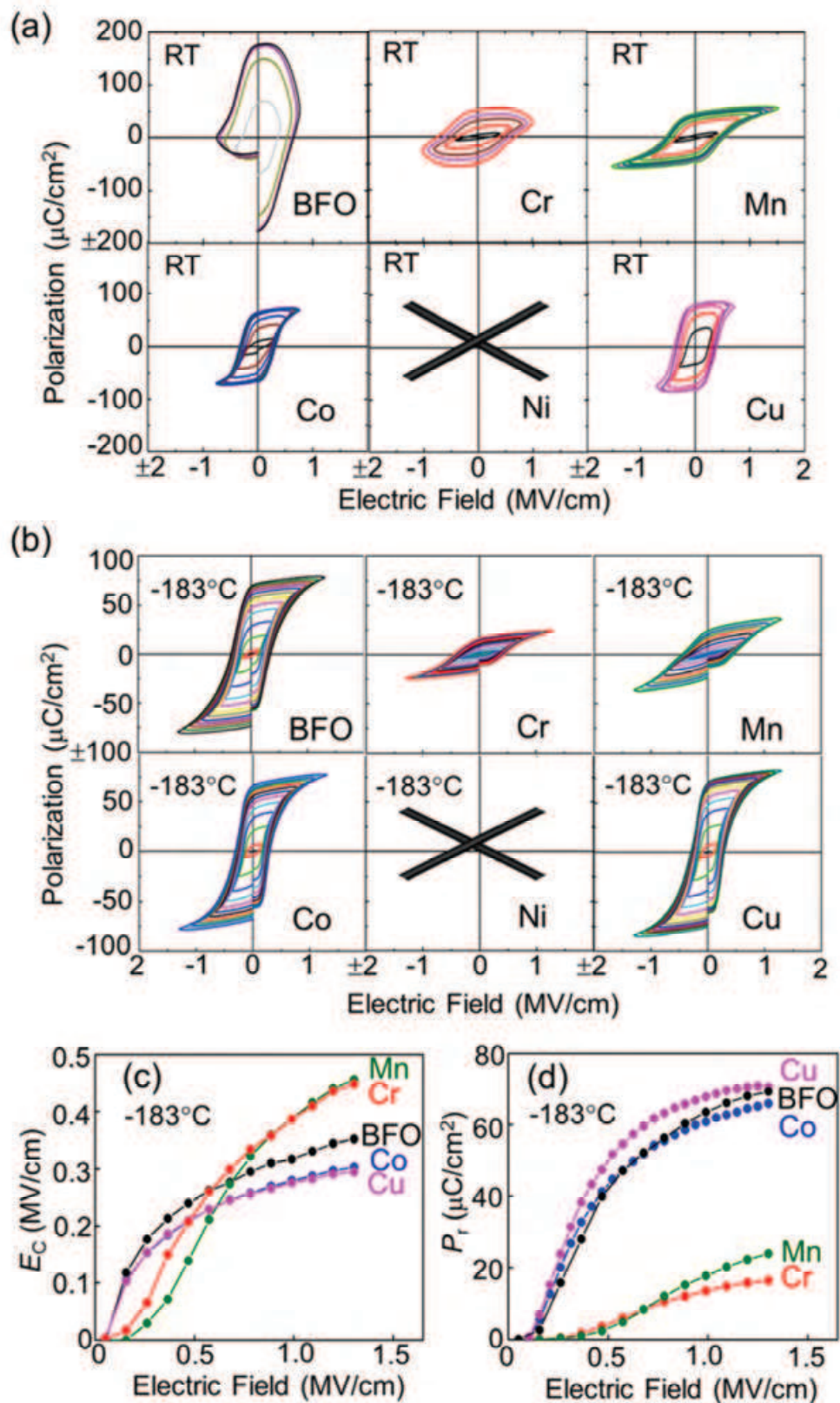
Fig. 18. Ferroelectric hysteresis loops of the Bi($M_{0.05}$Fe$_{0.95}$)O$_3$ films measured at RT using the ferroelectric tester with a 100 kHz driving system and measured at -183°C using a 2 kHz driving system.

MV/cm. Thus, Co and Cu substitution reduced the E_c of polycrystalline BiFeO$_3$ films without reducing P_r, which is suitable for memory and/or piezoelectric devices.

Figure 19 shows the magnetization curves of the Bi($M_{0.04}$Fe$_{0.96}$)O$_3$ films measured at RT. As mentioned in the previsou section, the pure BiFeO$_3$ films showed small magnetization. However, the substitution of Co, Ni, and Cu caused an increase in the magnetization, indicating substitution of these TM into the *B* sites of Fe, although it was not clear whether all the TMs were substituted into the *B*-sites. In the case of Co-substituted BiFeO$_3$, there was an increase in magnetization accompanied by the appearance of spontaneous magnetization and the coercive field of 2 kOe was observed at RT. In addition, according to other report, (Zhang *et al.*, 2010) clear observation of the magnetic domain structure using magnetic force microscopy (MFM) at RT was observed in 4 at.% Co-substituted BiFeO$_3$ has been reported. Based on these results, the increased magnetization in Co-substituted BiFeO$_3$ was confirmed by both macroscopic and local measurement methods.
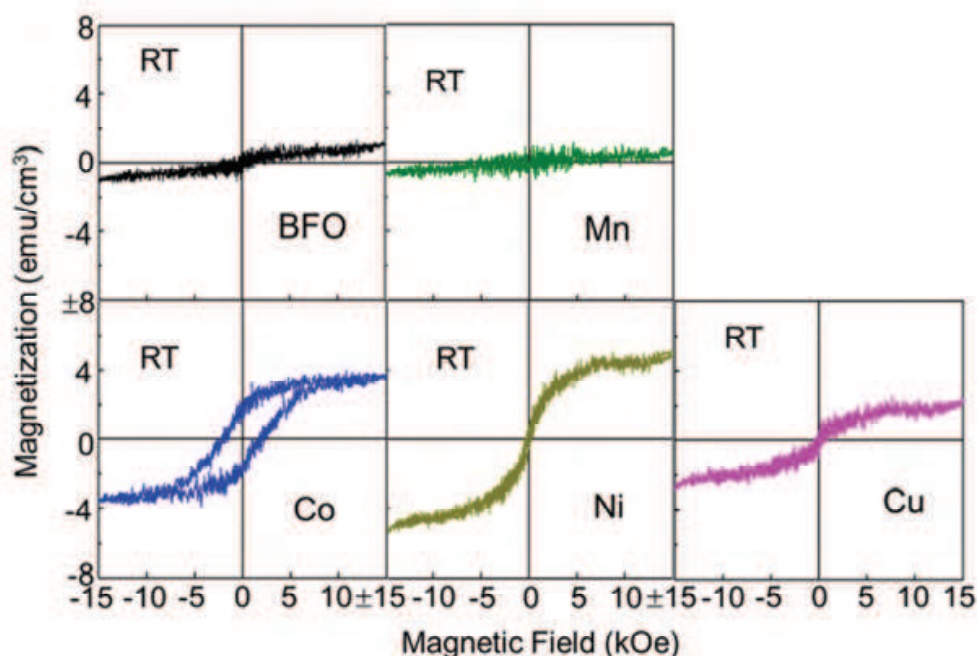

Fig. 19. Magnetization curves of the Bi($M_{0.05}$Fe$_{0.95}$)O$_3$, *M*= Cr, Mn, Co, Ni, and Cu] films measured at RT.

Cross-sectional TEM observation was carried out in order to clarify the influence of magnetic impurities on spontaneous magnetization in Co-substituted BiFeO$_3$ films. (Naganuma *et al.*, JMSJ 2009) Co-substituted BiFeO$_3$ film was deposited on a Pt/Ti/SiO$_2$/Si (100) substrate having a relatively flat surface. Grains of approximately hundreds of nm in size were formed. [Fig. 20(a)] Obvious secondary phases could not be observed in the wide area images. Figure 20(b) shows the NBD patterns for the [-1 3 -2] direction of the Co-substituted BiFeO$_3$ layer. Analysis of the NBD pattern shows that the crystal symmetry is rombohedral with a *R*3c space group, and the lattice parameters are *a* = 0.55 nm, *c* = 1.39 nm. The high-resolution TEM image around the grain boundary is shown in Fig. 20(c). Grain boundary formation is evident but the grain boundary phases could not be observed in this film. Therefore, it can be inferred that Co was substituted for Fe in BiFeO$_3$, and the magnetization enhancement might not be attributed to magnetic impurity phases. It was

concluded that the substitution of small of Co into the *B*-sites of $BiFeO_3$ could improve the leakage current property, reduce the electric coercive field without degrading the remanent polarization, and induce spontaneous magnetization at RT.
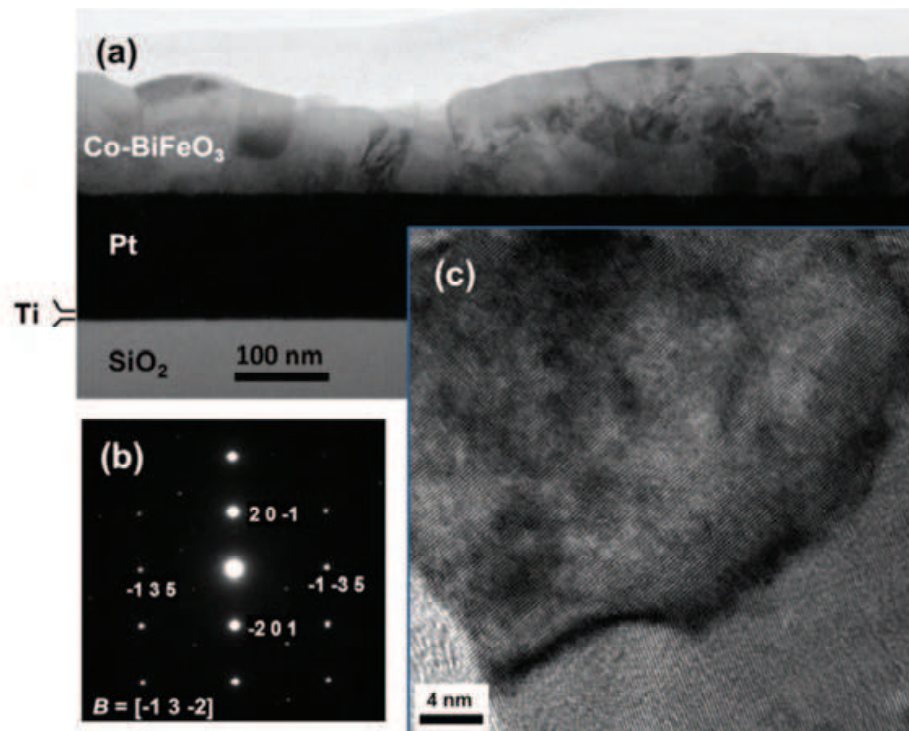

Fig. 20. Cross sectional TEM images of polycrystalline $Co\text{-}BiFeO_3$ film.

4. Multifunctional characteristics of BiCoO₃-BiFeO₃ solid solution epitaxial films

As clarified in the third section, the 4 or 5 at.%-Co-substituted $BiFeO_3$ polycrystalline films exhibited excellent electrical and magnetic characteristics. Substitution with larger amounts of Co was expected to result in further enhancement of the electrical and magnetic properties. It should be noted that high-pressure behavior becomes dominant in the highly Co-substituted $BiFeO_3$ films due to the high-pressure phase of $BiCoO_3$. In fact, a maximum of approximately 8 at.% Co can be substituted for Fe in the case of polycrystalline films while maintaining a single phase, whereas secondary phases of BiO_x are formed at Co concentrations above 8 at.%. (Naganuma *et al.*, JAP 2008) Because the character of $BiCoO_3$ is strongly influenced at high Co-substitution, hereafter, we refer to highly Co-substituted $BiFeO_3$ films as $BiCoO_3\text{-}BiFeO_3$. In one of our studies, (Naganuma *et al.*, JAP 2009) the high-pressure phase of $BiMnO_3$ was successfully stabilized in a thin-film form by using epitaxial strain. In accordance with this study, solid solution films of $BiCoO_3\text{-}BiFeO_3$ having a high $BiCoO_3$ content could also be stabilized on $SrTiO_3$ (100) single crystal substrates by epitaxial strain. In this section, the structural, (Yasui *et al.*, JJAP 2007) ferroelectric, (Yasui *et al.*, JJAP 2008, Yasui *et al.*, JAP 2009) and magnetic properties (Naganuma *et al.*, JAP 2011) of epitaxial $BiCoO_3\text{-}BiFeO_3$ films grown on $SrTiO_3$ substrates up to a $BiCoO_3$ concentration of ~58 at.% are systematically investigated.

The $BiFeO_3 - BiCoO_3$ solid solution films were grown on $SrTiO_3$ (100) substrates at 700°C by metalorganic chemical vapor deposition (MOCVD) established in Funakubo laboratory, and

Bi[(CH$_3$)$_2$-(2 – (CH$_3$)2NCH$_2$C$_6$H$_4$)], Fe(C$_2$H$_5$C$_5$H$_4$)$_2$, Co(CH$_3$C$_5$H$_4$)$_2$ and oxygen gas was used as the source materials. A vertical glass type reactor maintained at a pressure of 530 Pa was used for the film preparation. The films were deposited by MOCVD using pulse introduction of the mixture gases with Bi, Fe, and Co sources (pulse-MOCVD). The thickness of these films was approximately 200 nm. (Yasui *et al.*, JJAP 2007) The crystal structure of the deposited films was characterized by high-resolution XRD (HRXRD) analysis using a four-axis diffractometer (Philips X'-pert MRD). HRXRD reciprocal space mapping (RSM) around SrTiO$_3$ 004 and 204 was employed for a detailed analysis of crystal symmetry. The cross-sectional TEM (Hitachi HF-2000) observation working at 200 kV was used for microstructural analysis. The crystal symmetry was also identified using Raman spectroscopy by K. Nishida. (Yasui *et al.*, JJAP 2007) Raman spectra were measured using a subtractive single spectrometer (Renishaw SYSTEM1000) with a backward scattering configuration. A laser beam was focused on the film surface, and the beam spot was approximately 1 µm. The measurement time was fixed at 100 s. The leakage current v.s. electrical field and *P-E* loops were measured with a semiconductor parameter analyzer (HP4155B, Hewlett-Packard) and ferroelectric tester (TOYO Corporation, FCE-1A). The magnetic properties were measured in the in-plane direction using SQUID.

Figure 21 shows the typical θ/2θ and pole-figure HRXRD profiles of BiFeO$_3$ – BiCoO$_3$ solid solution films (BiCoO$_3$ concentrations of 0, 16, 21, and 33 at.%) grown on SrTiO$_3$ (100) substrates. Although Bi$_2$O$_3$ of secondary phase has a tendency to be formed at a high BiCoO$_3$ concentration, the single phase of BiFeO$_3$ – BiCoO$_3$ was successfully obtained by optimizing preparation conditions. The pole-figure HRXRD profiles indicate that all the films were epitaxially grown on SrTiO$_3$ (100) substrates. The magnified θ/2θ XRD profiles around BiFeO$_3$ – BiCoO$_3$ 002 indicate that the 002 peak shifted to high angle upon increasing the BiCoO$_3$ concentration, which indicates that the lattice constant for the out-of-plane direction approximated that of the SrTiO$_3$ substrates at high BiCoO$_3$ concentration.
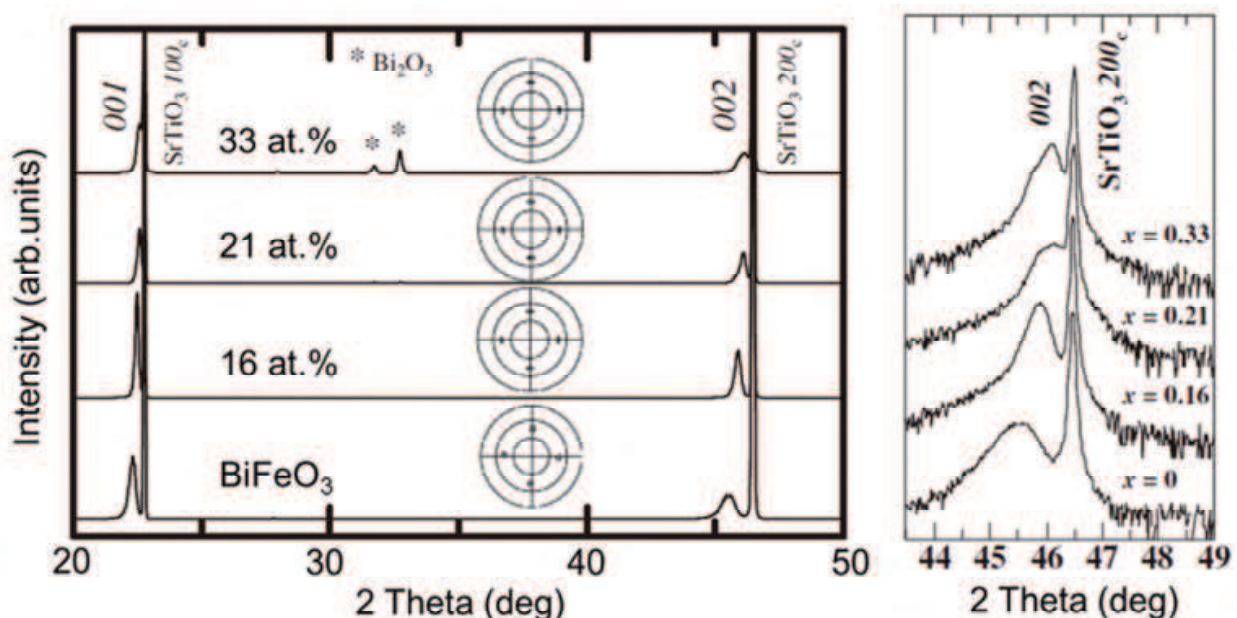

Fig. 21. θ/2θ and pole-figure HRXRD profiles of BiFeO$_3$ – BiCoO$_3$ solid solution films (BiCoO$_3$ concentration of 0, 16, 21, and 33 at.%) grown on SrTiO$_3$ (100) substrates.

The structures of the bulk forms of BiFeO$_3$ and BiCoO$_3$ are rombohedral and tetragonal, respectively. Conventional θ/2θ XRD measurement cannot be used to identify whether the crystal symmetry is rombohedral or tetragonal in the case of the BiFeO$_3$ – BiCoO$_3$ solid solution films. Therefore, HRXRD-RSM measurements around SrTiO$_3$ 004 and 204 were employed in the investigation of the crystal symmetry of the films. [Fig. 22] The pure BiFeO$_3$ film exhibited rhombohedral/monoclinic symmetry, as indicated by the existence of two asymmetric 204 spots in Fig. 22(b) and only one center spot of 004 in Fig. 22(a). This result is in agreement with that reported by Saito *et al.* for epitaxial BiFeO$_3$ films grown on SrRuO$_3$ (100)/SrTiO$_3$ (100) substrates. (Saito *et al.*, JJAP 2006) On the other hand, only single 204 and 004 spots were found for the film with a BiCoO$_3$ of 33 at.% [Figs. 22(g) and 22(h)], which indicates tetragonal crystal symmetry. Figures 22(c), 22(d), 22(e), and 22(f) show the HRXRD-RSM profiles for the films with 16 and 21 at.% BiCoO$_3$, respectively. Three peaks including one parallel spot and two tilting spots with a SrTiO$_3$ [001] orientation for 204, in both films, represented the existence of a mixture of (rhombohedral/monoclinic) and tetragonal symmetries.
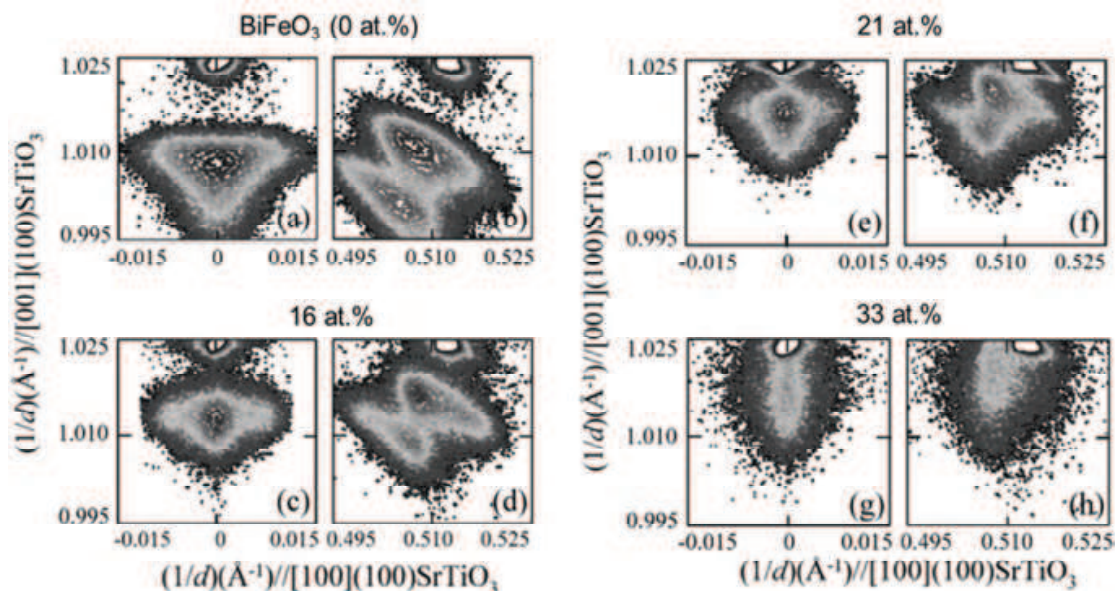

Fig. 22. HRXRD-RSM measurements around SrTiO$_3$ 004 and 204.

Raman spectroscopy was carried out in order to precisely check the change in crystal symmetry by K Nishida. (Yasui *et al.*, JJAP 2007) Raman spectra of the BiFeO$_3$-BiCoO$_3$ films and that of the SrTiO$_3$ substrate are shown in Fig. 23. The SrTiO$_3$ substrate shows a peak at 81 cm^{-1}, which is shifted to a value within 75-78 cm^{-1} for the films with 0-33 at.% BiCoO$_3$. It was confirmed that the peak observed for the films does not originate from the SrTiO$_3$ substrate. The decrease in the intensity of the SrTiO$_3$ peak with increasing film thickness for pure BiFeO$_3$ and the disappearance of the peak at ~600 cm^{-1}, as shown in Fig. 23, are also in agreement with the above results. The typical rhombohedral symmetry observed for bulk BiFeO$_3$ was indicated for the pure BiFeO$_3$ film and 16 at.% BiCoO$_3$ film. Different patterns with rhombohedral symmetry were observed for the film with 33 at.% BiCoO$_3$, which was shown to have tetragonal symmetry from the analysis of the HRXRD-RSM data. Furthermore, this peak of film was very similar to that of BiCoO$_3$ powder which has been confirmed to have tetragonal symmetry. For the films with 21 at.% BiCoO$_3$, it was ascertained from Fig. 23 that

the tetragonal and rhombohedral symmetries coexisted, which is almost consistent with the findings of the HRXRD-RSM experiment. It was revealed that the phase transition in $BiFeO_3$ – $BiCoO_3$ from (rhombohedral/monoclinic) symmetry to tetragonal symmetry is similar to the morphotropic phase boundary (MPB) in $Pb(Zr_xTi_{1-x})O_3$.

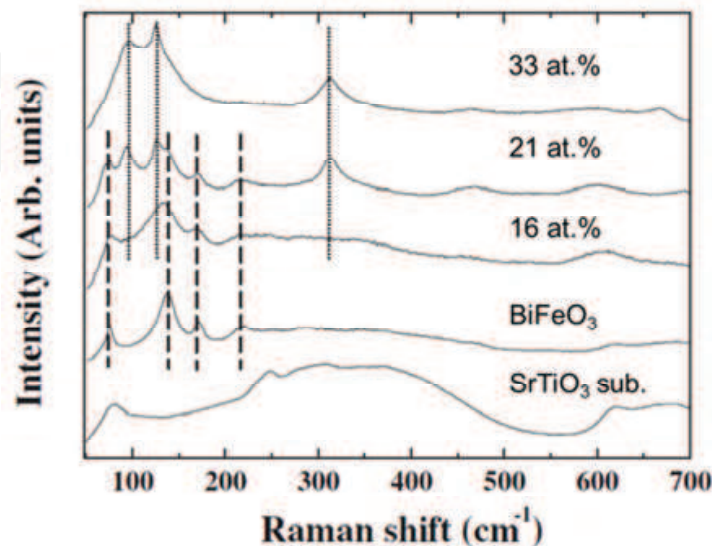Fig. 23. Raman spectra of the $BiFeO_3$-$BiCoO_3$ films and the $SrTiO_3$ substrate

Figure 24 shows the leakage current v.s. electrical field measurements taken at RT and *P-E* hysteresis loops measured at -193°C for the $BiFeO_3$-$BiCoO_3$ films. The leakage current
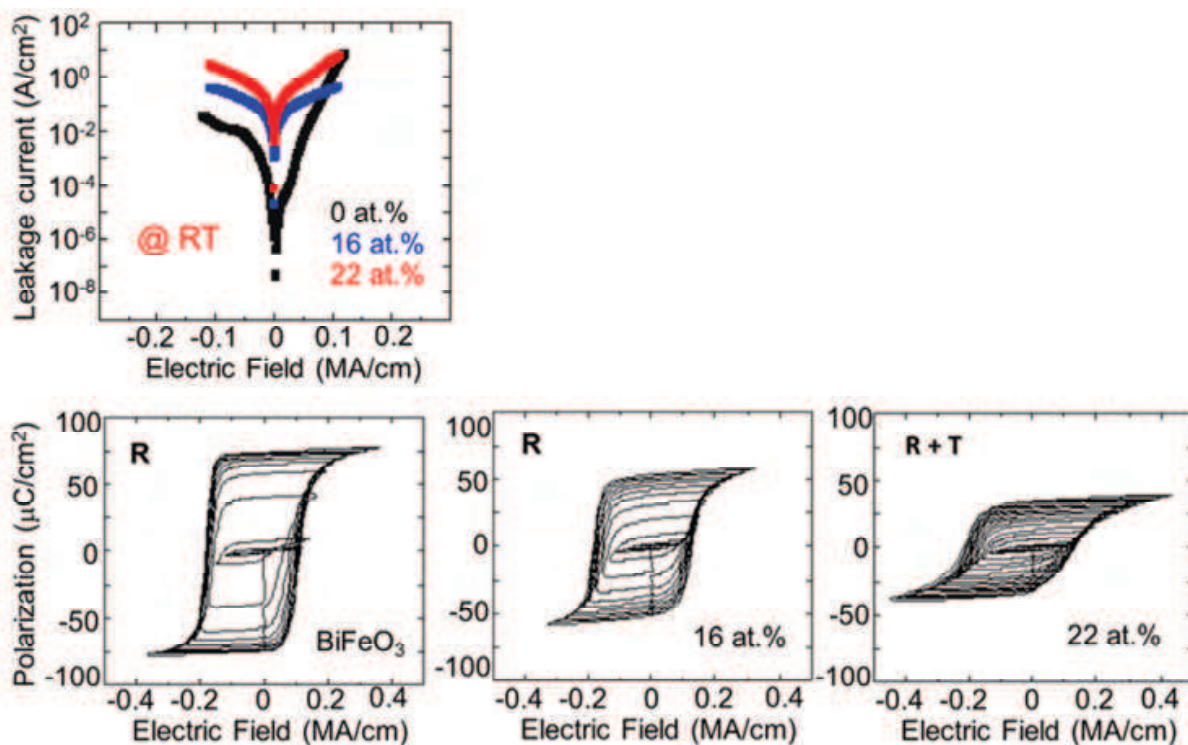
Fig. 24. Leakage current vs electric field measured at RT and *P-E* hysteresis loops measured at -193°C for the $BiFeO_3$-$BiCoO_3$ epitaxial films.

density at RT was very large for the BiFeO$_3$-BiCoO$_3$ films with high BiCoO$_3$ concentration, and the leakage current density increased with increasing BiCoO$_3$ concentration. Because of the magnitude of the leakage current at a BiCoO$_3$ concentration of 33 at.%, a leakage current measurement could not be evaluated for this film at RT using the semiconductor parameter analyzer. Although the previous discussions indicated that a small amount of Co-substitution can effectively reduce the leakage current, it can be seen from these that a large amount of Co-substitution degraded the leakage current property. In order to reduce the influence of leakage current density on the *P-E* hysteresis measurement for samples having a high BiCoO$_3$ concentration, the *P-E* loops were measured at a low temperature of -193°C. The *P-E* loops observed at -193°C were of relatively high squareness and the influence of leakage current density on the *P-E* loops could be successfully excluded at this temperature, except for the BiCoO$_3$ concentration of 33 at.%. At -193°C, spontaneous polarization decreased, and the coercive field of BiFeO$_3$-BiCoO$_3$ films increased with increasing BiCoO$_3$ concentration.

In the case of films with weak ferromagnetism such as BiFeO$_3$ films on substrates, eliminating the magnetization of the substrates from the films is important for acurrate evaluation of the magnetic properties of the films. Therefore, here, the magnetic properties of SrTiO$_3$ substrates were carefully evaluated. Figure 25(a) shows the *M-H* curves for two different weights of SrTiO$_3$ substrates. The SrTiO$_3$ substrates show a negative slope due to dimagnetism. The magnetization at 50 kOe (M_{50kOe}) for various weights of the SrTiO$_3$ substrates is plotted in Fig. 25(b). The absolute value of magnetization decreases with a decrease in the substrate weight, but some of the magnetization is retained even at zero weight. This retained magnetization is considered to be the background caused by the straw of the sample holder. In this study, standard straws produced by Quantum Design Inc. were used. Figure 25(c) shows the *M-H* curves of the SrTiO$_3$ substrate (weight = 0.0471 g) at 10 and 300 K. The hysteresis was not observed near the zero-field even at 10 K, indicating low magnetic impurity in the SrTiO$_3$ substrates and sample holder. The temperature dependence of M_{50kOe} is shown in Fig. 25(d). The diamagnetism slope decreased slightly with the temperature, however, it was not strongly influenced by the temperature. In this study, the magnetic properites of the films were carefully evaluated by eliminating SrTiO$_3$ substrate magnetization, and the same sample holder was used in all the magnetic measurements to exclude the effect of differences among straws.

Figure 26 shows the *M-H* curves measured at 300 K and the corresponding magnetic parameters that were estimated from the *M-H* curves. For pure BiFeO$_3$, the magnetization increased linearly at a high magnetic field. [Fig. 26(a)] Small hysteresis was observed near the zero fields, which is relatively obvious compared with that of polycrystalline BiFeO$_3$ films. [Fig. 15] For BiCoO$_3$ concentrations of 18–25 at.%, magnetization was clearly enhanced, and H_c was observed. [Figs. 26(b) and 26(c)] For a BiCoO$_3$ concentration of 58 at.%, the *M-H* curve was almost identical to that of pure BiFeO$_3$ films. There is an apparent linear increase in the magnetization at high-magnetic field for all the specimens. It was reported that by substituting *A*-site Bi ions in bulk BiFeO$_3$ with Gd or Nd, spontaneous magnetization was observed, and the magnetization increased linearly in the high-magnetic field region, which is in agreement with our results. Although it is difficult to accurately evaluate the slope at a high field due to film form, it can be considered that the antiferromagnetic spin structure still remained after substitution at the *A*- or *B*-site. The magnetic parameters M_{50kOe}, remanent magnetization (M_r), and coercive field (H_c),

estimated from the *M-H* curves are shown in Figs. 26(d) - 26(g). M_{10kOe} for polycrystalline $BiCoO_3$-$BiFeO_3$ films is also plotted in Fig. 26(e). The acronyms M_{50kOe} and M_{10kOe} indicate the magnetization at 50 kOe and 10 kOe, respectively. It was revealed that the M_{50kOe}, M_r, and H_c values increased with the $BiCoO_3$ concentration in the rhombohedral structure. This indicates the formation of ferro-like magnetic ordering. M_{50kOe}, M_r, and H_c were maximally enhanced at MPB composition. For a $BiCoO_3$ concentration above 30 at.%, corresponding to a tetragonal structure, M_{50kOe}, M_r, and H_c showed a tendency to decrease. These results indicate that the enhancement of the magnetic ordering in the MPB cannot be explained simply by ferrimagnetism in a double-perovskite structure, because maximum magnetization does not take place at the half-composition. In addition, the clear relationship between the change in the magnetization and the phase transition shows that the enhancement of magnetization was not attributable to magnetic impurities.
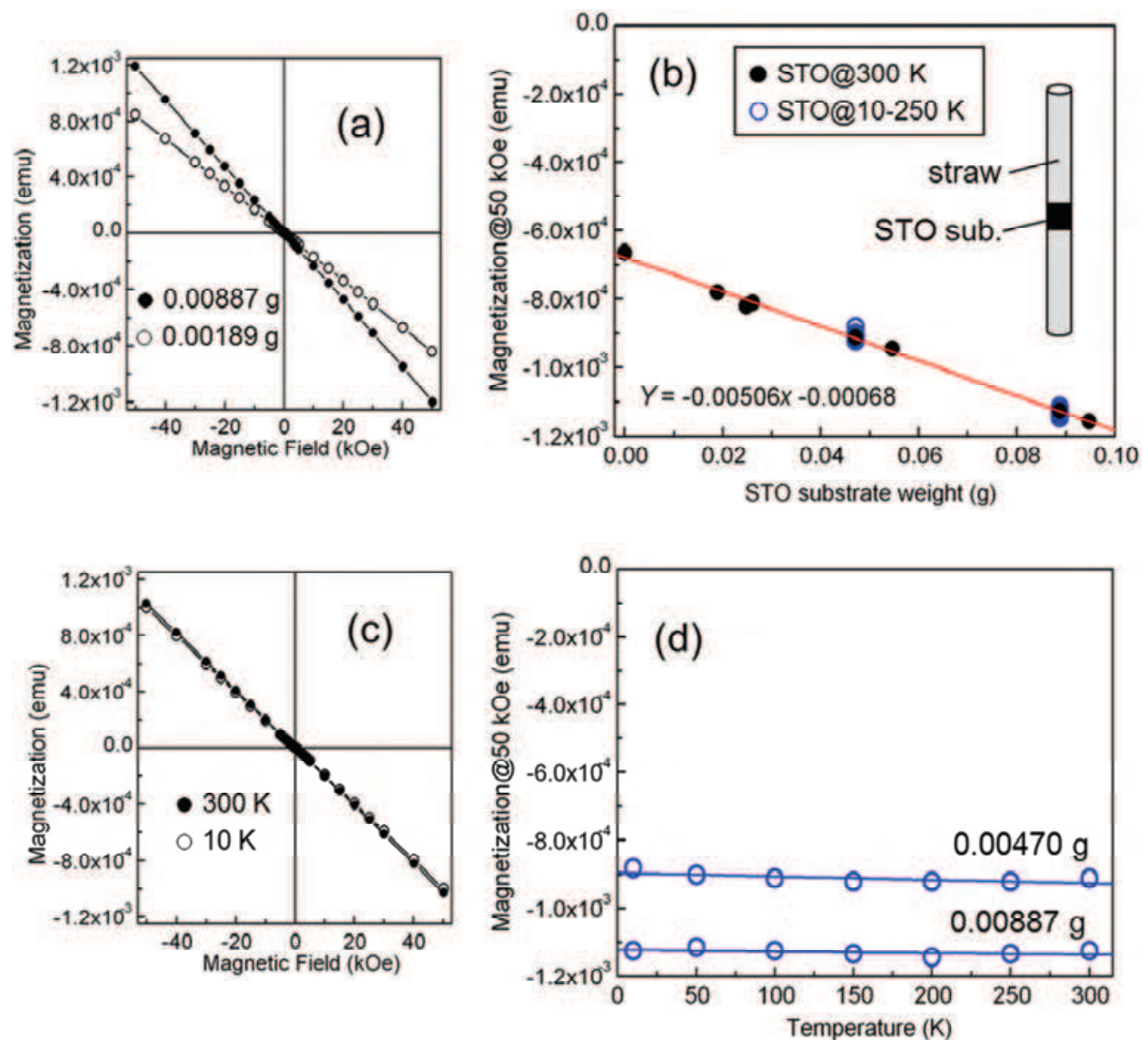

Fig. 25. $SrTiO_3$ substrate weight dependence of magentization ar 300 K, (a, b), and temperatuer dependence of magnetization of $SrTiO_3$ substrate with 0.00471 g (c, d).
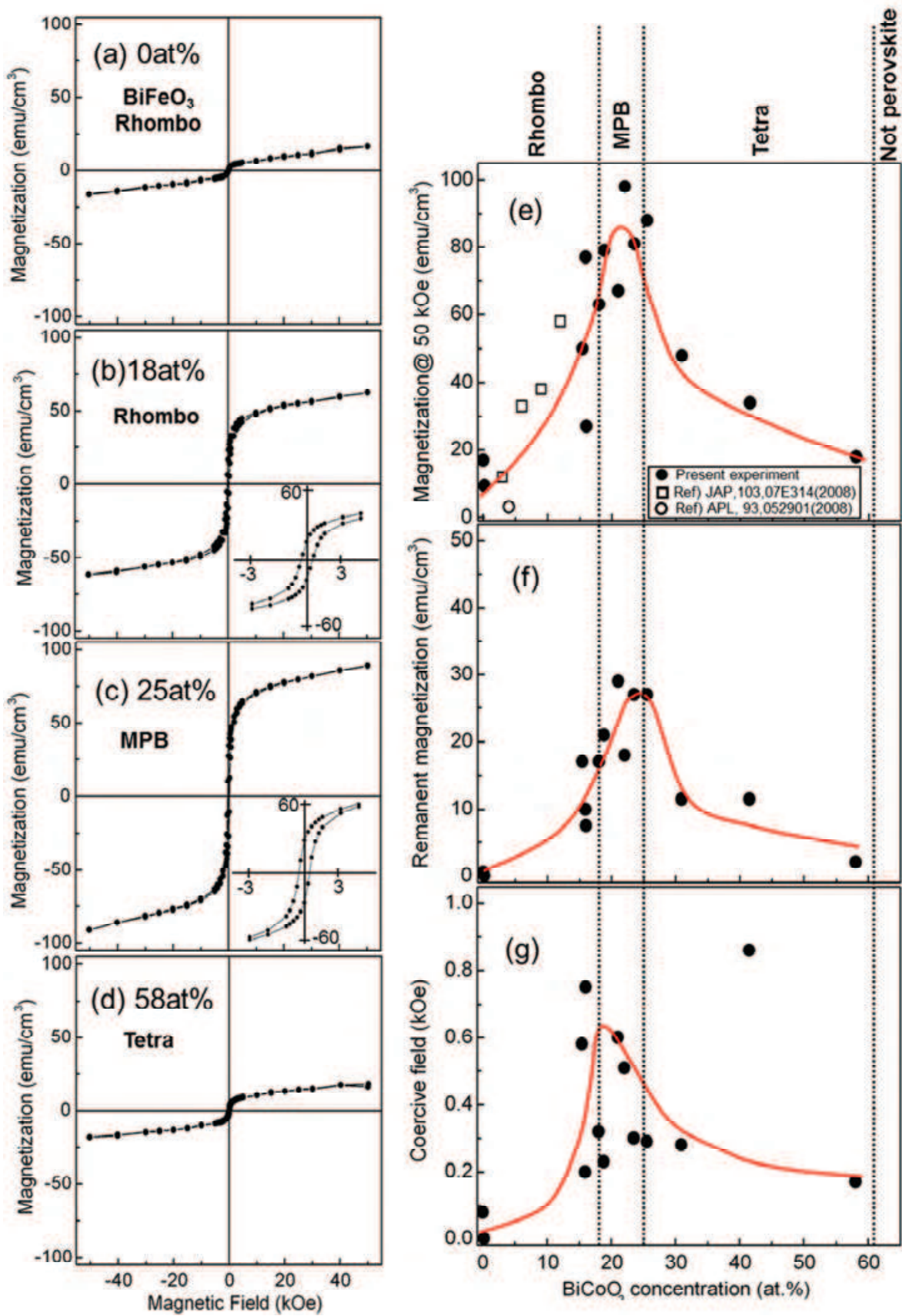
Fig. 26. *M-H* curves and corresponding magnetic parameters at 300 K.

Figure 27(a) and 27(b) show the M-H curves for 300 and 10 K for the $BiFeO_3$–$BiCoO_3$ film with 15 at.% of $BiCoO_3$ concentration. Interestingly, the slope at high magnetic field became larger when decreased the temperature to 10 K. Figure 27(c) shows the temperature dependence M_{50kOe}, M_r, and H_c. M_{50kOe} and M_r increased with decreasing temperature; however, these were not show strong temperature dependence. In contrast, H_c clearly increased with decreasing temperature.

Because $BiFeO_3$ and $BiCoO_3$ are synthesized under atmospheric pressure and a very high pressure phase, respectively, it is possible that the formation of magnetic impurities such as Co, $CoFe_2O_4$, and Fe_3O_4 $etc.$, may adversely affect the magnetic properties at high concentrations of $BiCoO_3$. In our previous studies, apparent magnetic impurities were not observed in the XRD measurement; however, nanosized magnetic particles are difficult to detect by XRD measurements. The superparamagnetic limit is a few nanometers in diameter for Co, $CoFe_2O_4$, and Fe_3O_4 $etc.$ Particles with such small sizes can be detected by TEM. Therefore, the microstructure of the film was confirmed by a cross-sectional TEM observation for a $BiCoO_3$ concentration of 17 at.%. [Fig. 28] No obvious magnetic impurities were observed in the TEM image, [Fig. 28(a)] and there was no diffraction spot attributed to magnetic impurities in the NBD pattern. [Fig. 28(b)] Our previous studies on nanoparticles suggest that particles that are a few nanometers in size can be confirmed by NBD, indicating that the influence of magnetic impurities might be ignored in our discussion. Although a further detailed investigation of the microstructure by high-resolution TEM observation is necessary, the enhancement of the magnetic properties might be attributable to ferro-like magnetic ordering.
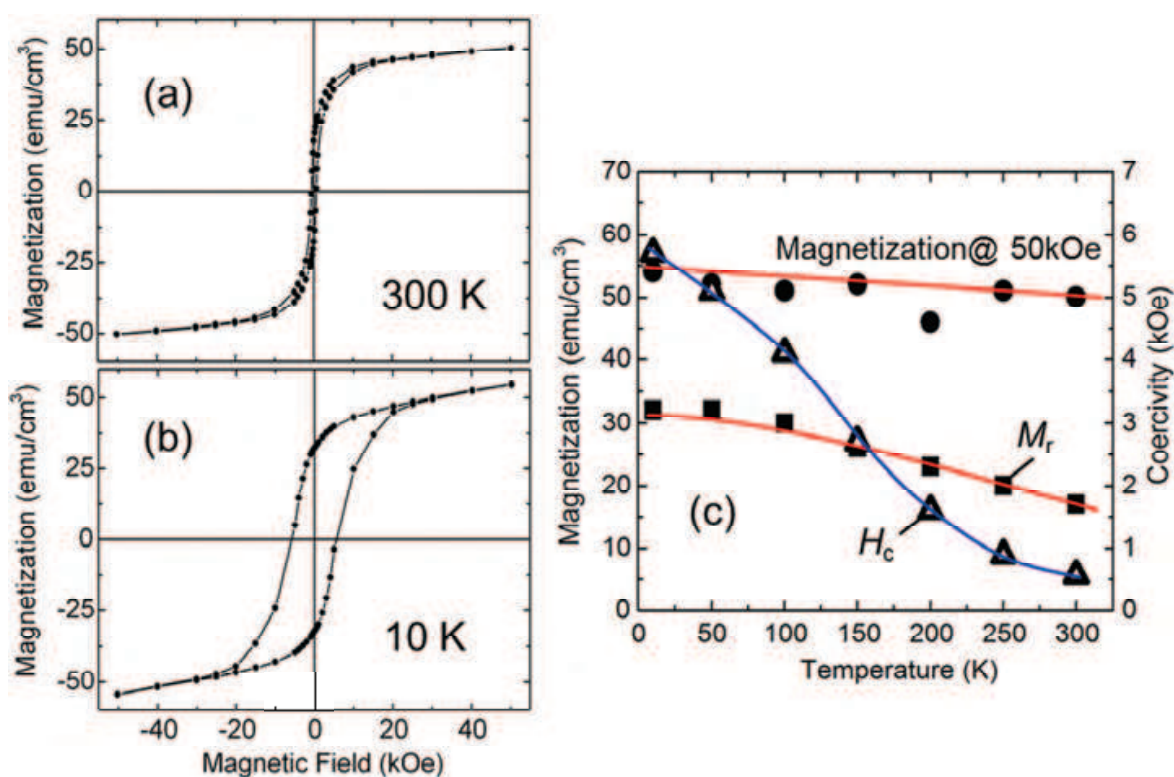

Fig. 27. M-H curves for 300 (a) and 10 K (b) for the $BiFeO_3$–$BiCoO_3$ film with 15 at.% of $BiCoO_3$ concentration, and temperature dependence of magnetization at 50 kOe (M_{50kOe}), remanent magnetization (M_r), and coercivity (H_c) (c).
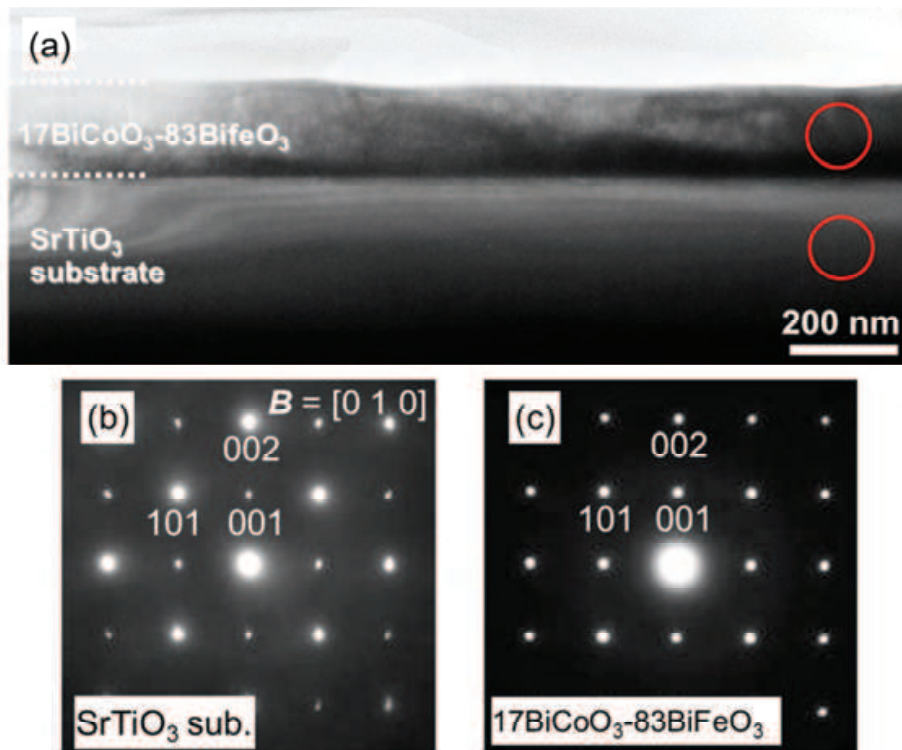
Fig. 26. Cross-sectional TEM observation for film with BiCoO₃ concentration of 17 at.%.

Here, we briefly discuss about possibility of the magneto-electric (ME) effect at RT in BiCoO₃–BiFeO₃ solid solution. As mentioned above, the magnetization of BiCoO₃–BiFeO₃ films was enhanced with rombohedral structure at a BiCoO₃ concentration below 18 at.%. In previous report, (Chu *et al*., 2008) for BiFeO₃ with rombohedral structure, a strong coupling was reported between the ferroelectric domains of rhombohedral 71° and 109° and the antiferromagnetic domains, and the anitiferromagnetic domains were reversed by ferroelectric switching at RT. In accordance with this BiFeO₃ regime, the BiCoO₃–BiFeO₃ films below BiCoO₃ concentration 18 at.% can potentially exhibit the ME effect with a macroscopic magnetization change because the rhombohedral domains exist at BiCoO₃ concentration below 18 at.%. The macroscopic magnetization changes operated at RT are useful in spintronics applications such as multi-valued memory using a spin-filter device *etc*. To confirm the ME effect, we will clarify the role of the substitution of Fe atom for Co atom and the origin of the enhanced magnetization in BiCoO₃–BiFeO₃ films. In addition, we expect to observe the magnetization changes driven by the electric field as well as external pressure in the MPB (BiCoO₃ concentration of 20 – 25 at.%) because the MPB phase shows a large displacement due to a large piezoelectric effect.

5. Conclusion

High quality single phase BiFeO₃ polycrystalline films with a space group of *R*3c were fabricated on Pt/Ti/SiO₂/Si (100) substrates. The leakage current density of the films at RT was large and strongly affected the ferroelectric measurement. The ferroelectric measurement was carried out at low temperature to reduce the leakage current, and a large polarization of 89 μC/cm² and a coercive field of 0.31 MV/cm were observed. The magnetic properties at RT were primarily due to antiferromagnetism. The magnetic properties at RT

were drastically enhanced by substitution of Fe in $BiFeO_3$ with 4 at % Co, which implies the induction of ferro-like magnetic ordering. The large leakage current and coercive field were simultaneously successfully reduced by substitution of Fe with 5 at.% Co. Epitaxial strain was employed in the preparation of films with high levels of Co substitution for Fe in $BiFeO_3$ because, under these conditions, the high-pressure phase of $BiCoO_3$ dominates stability. (hereafter, we refer to hese highly Co-substituted. $BiFeO_3$ films as $BiCoO_3$-$BiFeO_3$). The magnetization of the $BiCoO_3$-$BiFeO_3$ films increased drastically with an increase in the $BiCoO_3$ concentration, and the maximum magnetization was observed at 20-25 at.% substitution. Above a $BiCoO_3$ concentration of 25 at.%, there is a decrease in magnetization, which corresponds to the change from rhombohedral to tetragonal structural composition. Interestingly, the magnetization was maximally enhanced at the MPB of the rombohedral structure of $BiFeO_3$ and the tetragonal structure of $BiCoO_3$. It is well known that large piezoelectricity can be expected in the MPB; therefore, the cross-correlation between piezoelectricity and magnetism can be expected in the MPB. Furthermore, this material has the capacity possibility to show wide cross-correlation among magnetism, ferroelectricity, piezoelectricity, and optical properties. Epitaxial $BiCoO_3$-$BiFeO_3$ solid solutions can open up an avenue for the development of new multifunctional materials, may have potential application in devices such as multivalued memories, spin-filter devices, V-MRAM, magnetic/electric field tunability or flexibility, and piezoelectric materials with MPB *etc.*

6. Acknowledgements

7. References

Venevtsev, Y. N.; Zhadanow, G. & Solov'ev, S. (1960), *Soviet Physics Crystallography* Vol. 4, 1960, pp. 538.

Kiselev, S. V.; Ozerov, R. P. & Zhdanov, G. S. (1963) Detection of Magnetic Order in Ferroelectric $BiFeO_3$ by Neutron Diffraction, *Soviet Physics DOKLADY*. Vol 7, February 1963, pp. 742-743.

Kubel, F.; & Schmid, H. (1990) Structure of Ferroelectric and Ferroelastic Monodomain Crystal of the Perovskite BiFeO$_3$, *Acta Crystallography Sect. B: Structure*. Vol. 46, June 1990, pp. 698-702.

Ederer, C.; and Spaldin N. A. (2005) Effect of Epitaxial Strain on the Spontaneous Polarization of Thin Film Ferroelectrics, *Physical Review Letters*., Vol. 95, December 2005, pp. 257601-1-4.

Li, J.; Wang, J, Wuttig M., Ramesh, R.; Wang, N.; Ruette, B.; Pyatakov, A. P.; Zvezdin, A. K.; & Viehland, D.; (2004) Dramatically enhanced polarization in (001), (101), and (111) BiFeO$_3$ thin films due to epitiaxial-induced transitions, *Applied Physics Letters*, Vol. 84, June 2004, pp.5261-5263.

Yun, K. Y.; Ricinschi D.; Kanashima, T.; Noda, M.; & Okuyama, M.; (2004) Giant Ferroelectric Polarization Beyond 150 C/cm^2 in BiFeO$_3$ Thin Film, *Japanese Journal of Applied Physics Letters*, Vol. 43, April 2004, L647-648.

Naganuma, H.; & Okamura, S. (2007) Structural, magnetic, and ferroelectric properties of multiferroic BiFeO$_3$ film fabricated by chemical solution deposition, *Journal of Applied Physics*, Vol. 101, December 2007, pp. 09M103-1-3.

Pabst, G. W.; Martin, L. W.; Chu, Y. H.; & Ramesh, R. (2007) Leakage mechanisms in BiFeO$_3$ thin films, *Applied Physics Letters*, Vol. 90, February 2007 pp. 072902-1-3.

Ederer, C.; & Spaldin, N. A. (2005) Weak ferromagnetism and magnetoelectric coupling in bismuth ferrite, *Physical Review B*, Vol. 71, February 2005, pp. 060401(R)-1-4.

Zhao, T.; Scholl A.; Zavaliche F.; Lee K.; Barry, M.; Doran A.; Cruz, M. P.; Chu, Y. H.; Ederer C.; Spaldin, N. A.; Das, R. R.; Kim, D. M.; Baek, S. H.; Eom, C. B.; & Ramesh, R. (2006) Electrical control of antiferromagnetic domains inmultiferroic BiFeO$_3$ films at room temperature, *Nature Materials*, Vol. 5, September 2006, pp.823-829.

Dzyaloshinskii, I. E. (1957) *Soviet Physics JEPT*, Vol. 5, No. 6, February 1957, pp. 1259-1272.

Moriya, T. (1960) Anisotropic Superexchange Interaction and Weak Ferromagnetism, *Physical Review*, Vol. 120, May 1960, pp.91-98.

Sosnowska, I.; Peterlin-Neumaier, T.; & Streichele, E. (1982) Spiral Magnetic ordering in Bismuth Ferrite, *Journal of Physics C*, Vol. 15, January 1982, pp. 4835-4846.

Chu, Y.-H.; Martin, L. W.; Holcomb, M. B.; Gajek M.; Han, S.-J.; He, Q.; Balke, N.; Yang, C.-H.; Lee, D.; Hu, W.; Zhan, Q.; Yang, P.-L.; Fraile-Rodriguez, A.; Scholl, A.; Wang, S. X. & Ramesh ,R. (2008), Electric-field control of local ferromagnetism using a magnetoelectric multiferroic, *Nature Materials*, Vol. 7, April 2008, pp. 478-482.

Shima, H.; Kawae, T.; Morimoto, A.; Matsuda, M.; Suzuki, M.; Tadokoro, T.; Naganuma, H.; Iijima, T.; Nakajima, T. & Okamura, S. (2009) Optical Properties of BiFeO$_3$-System Multiferroic Thin Films, *Japanese Journal of Applied Physics*, Vol. 48, September 2009, pp. 09KB01-1-4.

Naganuma, H.; Kovacs, A.; Y. Hirotsu, Y. Inoue, and Okamura, S. (2007) Preparation and Characterization of Multiferroic BiFeO$_3$ Films, *Transactions of the Materials Research Society of Japan*, 2007, Vol. 32, pp. 39-42.

Naganuma, H.; Kovacs, A.; Hirata, A.; Hirotsu, Y. & Okamura, S., (2007) Structural Analysis of Polycrystalline $BiFeO_3$ Films by Transmission Electron Microscopy, *Materials Transaction*, Vol. 48, August 2007, pp. 2370-2373.

Naganuma, H.; Inoue. Y. & Okamura, S. (2007) Leakage Current Mechanism of Polycrystalline BiFeO3 Films with Pt Electrode, *Integrated Ferroelectrics*, Vol. 46, 2007, pp.6948-6951. ISSN 1058-4587.

Naganuma, H.; Inoue. Y. & Okamura, S. (2008) Dependence of Ferroelectric and Magnetic Properties on Measuring Temperatures for Polycrystalline $BiFeO_3$ Films, *IEEE Transactions on Ultrasonics, Ferroelectrics, and Frequency Control*, Vol. 55 No. 5, pp.1046-1050.

Naganuma, H.; Inoue. Y. & Okamura, S. (2008) Estimation of Leakage Current Density and Remanent Polarization of $BiFeO_3$ Films with Low Resistivity by Positive, Up, Negative, and Down Measurements, *Japanese Journal of Applied Physics*, Vol. 47, July 2008, pp.5558-5560.

Naganuma, H.; Inoue. Y. & Okamura, S. (2008) Evaluation of Electrical Properties of Leaky $BiFeO_3$ Films in High Electric Field Region by High-Speed Positive-Up–Negative-Down Measurement, *Applied Physics Express*, Vol. 1, pp.061601-1-3.

Naganuma, H.; Miyazaki, T.; Ukachi, A.; Oogane, M.; Mizukami, S. & Ando, Y. Structural characterization of epitaxial multiferroic $BiFeO_3$ films grown on $SrTiO_3$ (100) substrates by crystallizing amorphous $Bi–Fe–O_x$, *Journal of Ceramic Society of Japan*, Vol. 118, June 2010, pp. 648-651.

Naganuma, H.; Oogane, M. & Ando, Y. (2011) Exchange biases of Co, Py, $Co_{40}Fe_{40}B_{20}$, $Co_{75}Fe_{25}$, and $Co_{50}Fe_{50}$ on epitaxial $BiFeO_3$ films prepared by chemical solution deposition, *Journal of Applied Physics*,2011 in-press.

Kirkland, E. J.; *Advanced Computing in Electron Microscopy* (Plenum, New York, 1998).

Wang, J.; Neaton, J. B.; Zheng, H.; Nagarajan, V.; S. Ogale, B.; Liu, B.; Viehland, D.; Vaithyanathan, V.; Schlom, D. G.; Waghmare, U. V.; Spaldin, N. A.; Rabe, K. M.; Wuttig, M. & Ramesh, R. (2003) Epitaxial $BiFeO_3$ Multiferroic Thin Film Heterostructures, *Science* Vol. 299, February 2003, pp.1719-1722.

Yun, K. Y.; Noda, M.; Okuyama, M.; Saeki, H.; Tabata, H. & Saito, K. (2004) Structural and multiferroic properties of $BiFeO_3$ thin films at room temperature, *Journal of Applied Physics*, Vol. 96, May 2004, pp.3399-3403.

Naganuma, H.; Y. Inoue, & Okamura, S. (2010) Evaluation of ferroelectric hysteresis loops of leaky multiferroic $BiFeO_3$ films using a system with a high driving frequency of 100 kHz system, *Journal of Ceramics Society of Japan*, Vol. 118, June 2010, pp.656-658.

Bai, F.; Wang, J.; Wuttig, M.; Li, J. F.; Zvezdin, A. K.; Cross, L. E.; & Viehland, D.; (2005) Destruction of spin cycloid in $(111)_c$-oriented $BiFeO_3$ thin films by epitaxial constraint: Enhanced polarization and release of latent magnetization, *Applied Physics Letters*, Vol. 86, pp. 032511-1-3.

Lebeugle, D.; Colson, D.; Forget, A.; Viret, M.; Bonville, P.; Marucco, J. F. & Fusil S. (2007) Room-temperature coexistence of large electric polarization and magnetic order in $BiFeO_3$ single crystals, *Physical Review B*, Vol. 76, July 2007, pp. 024116-1-8.

Naganuma, H.; Miura, J. & Okamura, S. (2008) Ferroelectric, electrical and magnetic properties of Cr, Mn, Co, Ni, Cu added polycrystalline BiFeO₃ films, *Applied Physics Letters*, Vol. 93, August 2008, pp. 052901-1-3.

Naganuma, H.; Miura, J. & Okamura, S. (2009) Annealing temperature effect on ferroelectric and magnetic properties in Mn-added polycrystalline BiFeO₃ films, *Journal of Electroceramics*, Vol. 22, January 2008, pp.203-208.

Naganuma, H.; Shimura, N.; Miura, J.; Shima, H.; Yasui, S.; Nishida, K.; Katoda, T.; Iijima, T.; Funakubo, H.; & Okamura, S. (2008) Enhancement of ferroelectric and magnetic properties in BiFeO₃ films by small amount of cobalt addition, *Journal of Applied Physics*, Vol. 103, pp.07E314-1-3.

Naganuma, H.; Miura, J.; Nakajima, M.; Shima, H.; Okamura, S. Yasui, S.; Funakubo, H.; Nishida, K.; Iijima, T., Azuma, M.; Ando, Y.; Kamishima, K.; Kakizaki K.; & Hiratsuka, N. (2008) Annealing Temperature Dependences of Ferroelectric and Magnetic Properties in Polycrystalline Co-Substituted BiFeO₃ Films, *Japanese Journal of Applied Physics*, Vol. 47, pp. 7574-7578.

Naganuma, H.; Miura, J.; Kamishima, K.; Kakizaki, K.; Hiratsuka, N.; Ando, Y.; Okamura, S. (2009) Room Temperature Ferroelectric and Magnetic Properties of Multiferoic Cobalt Substituted Bi Ferrite Films, *Journal of Magnetic Society of Japan*, Vol. 33, pp. 237-241.

Zhang, Q.; Kim, C. H.; Jang, Y. H.; Hwang, H. J.; & Cho, J. H. (2010) *Applied Physics Letters*, Vol. 96, April 2010, 99. 152901-1-3.

Naganuma, H.; Kovacs, A.; Harima, T.; Shima, H.; Okamura, S.; & Hirotsu, Y. (2009) Structural analysis of interfacial strained epitaxial BiMnO₃ films fabricated by chemical solution deposition, *Journal of Applied Physics*, Vol. 105, March 2009, pp.07D915-1-3.

Yasui, S.; Nishida, K.; Naganuma, H.; Okamura, S.; Iijima, T. & Funakubo, H. (2007) Crystal Structure Analysis of Epitaxial BiFeO₃ – BiCoO₃ Solid Solution Films Grown by Metalorganic Chemical Vapor Deposition, *Japanese Journal of Applied Physics*, Vol. 46, October 2007, pp.6948-6951.

Yasui, S.; Naganuma, H.; Okamura, S.; Nishida, K.; Yamamoto, T.; Iijima, T.; Azuma, M.; Morioka, H.; Saito, K.; Ishikawa, M.; Yamada, T.; & Funakubo, H. (2008) Crystal Structure and Electrical Properties of {100}-Oriented Epitaxial BiCoO₃–BiFeO₃ Films Grown by Metalorganic Chemical Vapor Deposition, *Japanese Journal of Applied Physics*, Vol. 47, September 2008, pp.7582-7585.

Yasui, S.; Nakajima, M.; Naganuma, H.; Okamura, S.; Nishida, K.; Yamamoto, T.; Iijima, T.; Azuma, M.; Morioka, H.; Saito, K.; Ishikawa, M.; Yamada, T.; & Funakubo, H. (2009) Composition control and thickness dependence of {100}-oriented epitaxial BiCoO₃–BiFeO₃ films grown by metalorganic chemical vapor deposition, *Journal of Applied Physics*, Vol. 105, March 2009, pp.061620-1-5.

Naganuma, H.; Yasui, S.; Nishida, K.; Iijima, T.; Funakubo, H.; & Okamura, S. (2011) Enhancement of magnetization at morphotropic phase boundary in epitaxial BiCoO₃-BiFeO₃ solid solution films grown on SrTiO₃ (100) substrates by metalorganic chemical-vapor deposition, *Journal of Applied Physics*, in-press.

Saito, K.; Ulyanenkov, A.; Grossmann, V.; Ress, H.; Bruegemann, L.; Ohta, H.; Kurosawa, T.; Ueki, S.; & Funakubo, H. (2006) Structural Characterization of BiFeO$_3$ Thin Films by Reciprocal Space Mapping, *Japanese Journal of Applied Physics*. Vol. 45, September 2006, pp.7311-7314.

Ferroelectrics - Physical Effects

Edited by Dr. Mickaël Lallart

ISBN 978-953-307-453-5

Hard cover, 654 pages

Publisher InTech

Published online 23, August, 2011

Published in print edition August, 2011

Ferroelectric materials have been and still are widely used in many applications, that have moved from sonar towards breakthrough technologies such as memories or optical devices. This book is a part of a four volume collection (covering material aspects, physical effects, characterization and modeling, and applications) and focuses on the underlying mechanisms of ferroelectric materials, including general ferroelectric effect, piezoelectricity, optical properties, and multiferroic and magnetoelectric devices. The aim of this book is to provide an up-to-date review of recent scientific findings and recent advances in the field of ferroelectric systems, allowing a deep understanding of the physical aspect of ferroelectricity.

INTECH
open science | open minds